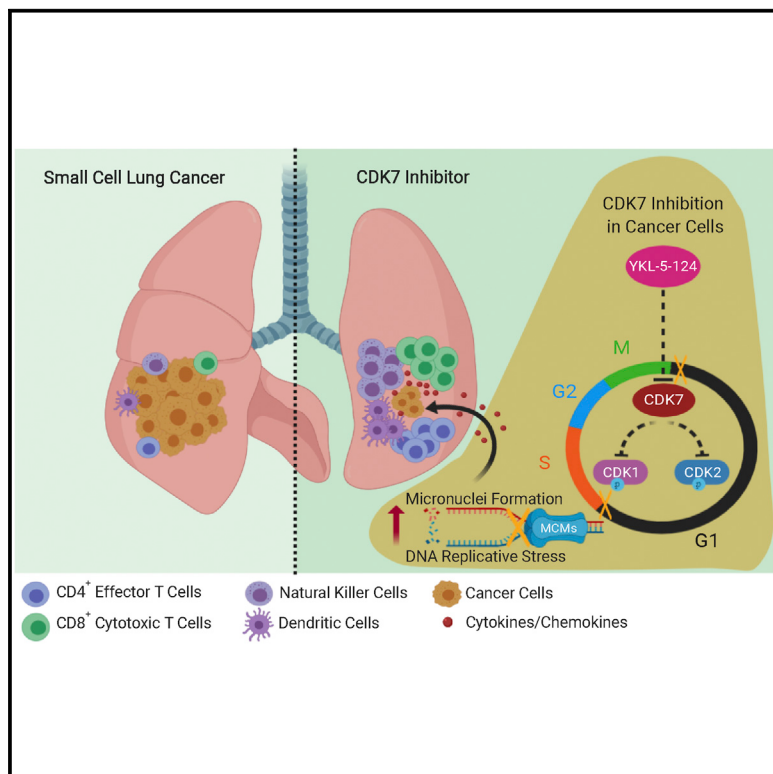


Cancer Cell

CDK7 Inhibition Potentiates Genome Instability Triggering Anti-tumor Immunity in Small Cell Lung Cancer

Graphical Abstract



Authors

Hua Zhang, Camilla L. Christensen,
Ruben Dries, ..., George Miller,
Nathanael S. Gray, Kwok-Kin Wong

Correspondence

hua.zhang@nyulangone.org (H.Z.),
nathanael_gray@dfci.harvard.edu
(N.S.G.),
kwok_kin.wong@nyulangone.org
(K.-K.W.)

In Brief

Zhang et al. show that selective CDK7 inhibition with YKL-5-124 disrupts the cell cycle and causes replicative stress, eliciting an inflammatory response. YKL-5-124 in combination with anti-PD-1 therapy reduces tumor growth and increases survival in mouse models of small cell lung cancer.

Highlights

- CDK7 inhibition impairs cell cycle and DNA replication and induces genome instability
- CDK7 inhibitor YKL-5-124 activates IFN- γ signaling and induces TNF- α and CXCL9/10
- YKL-5-124 provokes a robust immune program, which is further improved by anti-PD-1
- Combining YKL-5-124 with anti-PD-1 and chemotherapy improves tumor response

CDK7 Inhibition Potentiates Genome Instability Triggering Anti-tumor Immunity in Small Cell Lung Cancer

Hua Zhang,^{1,16,*} Camilla L. Christensen,^{2,16} Ruben Dries,^{3,16} Matthew G. Oser,^{2,16} Jiehui Deng,¹ Brian Diskin,⁴ Fei Li,¹ Yuanwang Pan,¹ Xuzhu Zhang,⁵ Yandong Yin,⁵ Eleni Papadopoulos,¹ Val Pyon,¹ Cassandra Thakurdin,¹ Nicholas Kwiatkowski,⁶ Kandarp Jani,² Alexandra R. Rabin,¹ Dayanne M. Castro,⁷ Ting Chen,¹ Heather Silver,¹ Qingyuan Huang,¹ Mirna Bulatovic,¹ Catriona M. Dowling,¹ Belen Sundberg,⁴ Alan Leggett,⁶ Michela Ranieri,¹ Han Han,¹ Shuai Li,¹ Annan Yang,² Kristen E. Labbe,¹ Christina Almonte,¹ Vladislav O. Sviderskiy,⁸ Max Quinn,¹ Jack Donaghue,¹ Eric S. Wang,⁶ Tinghu Zhang,⁶ Zhixiang He,⁶ Vamsidhar Velcheti,¹ Peter S. Hammerman,^{2,15} Gordon J. Freeman,⁹ Richard Bonneau,⁷ William G. Kaelin, Jr.,^{9,10} Kate D. Sutherland,^{11,12} Ariena Kersbergen,¹² Andrew J. Aguirre,^{2,13} Guo-Cheng Yuan,³ Eli Rothenberg,⁵ George Miller,⁴ Nathanael S. Gray,^{6,14,*} and Kwok-Kin Wong^{1,17,*}

¹Laura and Isaac Perlmutter Cancer Center, New York University Langone Medical Center, New York, NY 10016, USA

²Department of Medical Oncology, Dana-Farber Cancer Institute, Boston, MA 02215, USA

³Department of Pediatric Oncology, Dana-Farber Cancer Institute, Boston, MA 02215, USA

⁴S. Arthur Localio Laboratory, Department of Surgery, New York University School of Medicine, New York, NY 10016, USA

⁵Department of Biochemistry and Molecular Pharmacology, New York University School of Medicine, New York, NY 10016, USA

⁶Department of Cancer Biology, Dana-Farber Cancer Institute, Boston, MA 02215, USA

⁷Departments of Biology and Computer Science, Center for Genomics and Systems Biology, New York University, New York, NY 10010, USA

⁸Department of Pathology, New York University School of Medicine, New York, NY 10016, USA

⁹Department of Medicine, Brigham and Women's Hospital, Harvard Medical School, Boston, MA 02215, USA

¹⁰Howard Hughes Medical Institute, Chevy Chase, MD 20815, USA

¹¹Cancer Biology and Stem Cells Division, The Walter and Eliza Hall Institute of Medical Research, Parkville, VIC 3052, Australia

¹²Department of Medical Biology, The University of Melbourne, Parkville, VIC 3052, Australia

¹³Broad Institute of MIT and Harvard, Cambridge, MA 02142, USA

¹⁴Department of Biological Chemistry and Molecular Pharmacology, Harvard Medical School, Boston, MA 02215, USA

¹⁵Present address: Novartis Institutes for Biomedical Research, Cambridge, MA 02139, USA

¹⁶These authors contributed equally

¹⁷Lead Contact

*Correspondence: hua.zhang@nyulangone.org (H.Z.), nathanael_gray@dfci.harvard.edu (N.S.G.), kwok_kin.wong@nyulangone.org (K.-K.W.)
<https://doi.org/10.1016/j.ccr.2019.11.003>

SUMMARY

Cyclin-dependent kinase 7 (CDK7) is a central regulator of the cell cycle and gene transcription. However, little is known about its impact on genomic instability and cancer immunity. Using a selective CDK7 inhibitor, YKL-5-124, we demonstrated that CDK7 inhibition predominately disrupts cell-cycle progression and induces DNA replication stress and genome instability in small cell lung cancer (SCLC) while simultaneously triggering immune-response signaling. These tumor-intrinsic events provoke a robust immune surveillance program elicited by T cells, which is further enhanced by the addition of immune-checkpoint blockade. Combining YKL-5-124 with anti-PD-1 offers significant survival benefit in multiple highly aggressive murine models of SCLC, providing a rationale for new combination regimens consisting of CDK7 inhibitors and immunotherapies.

Significance

Small cell lung cancer (SCLC) is one of the deadliest human cancers for which new treatment paradigms are urgently needed. Recently, immune-checkpoint blockade (ICB) with chemotherapy was approved for first-line therapy; however, the added survival benefit remains limited. Here, we demonstrate that CDK7 inhibition results in cell-cycle disruption and genomic instability while activating immune-response signaling in SCLC. This tumor cell-intrinsic effect potentiates activation of infiltrating immune cells, supporting a role of CDK7 in regulating anti-tumor immunity. Our results show that the CDK7 inhibitor YKL-5-124 increases the susceptibility of SCLC to anti-PD-1, and provides better survival in multiple murine SCLC models. Our data suggest that adding YKL-5-124 to ICB and chemotherapy may improve treatment efficacy and survival benefit in patients with SCLC.

INTRODUCTION

Small cell lung cancer (SCLC) is one of the deadliest human cancers, accounting for about 15% of all lung cancer (van Meerbeeck et al., 2011). It often arises in heavy smokers and is characterized by rapid growth and early metastasis (Bunn et al., 2016; Semenova et al., 2015). Although SCLC patients often initially respond to chemotherapy, tumors nearly always recur within 6–12 months, resulting in a 5-year survival rate of less than 7% (van Meerbeeck et al., 2011).

Immune evasion is a hallmark of cancer (Schreiber et al., 2011). Therapies to enhance anti-tumor immune response, particularly antibodies blocking inhibitory immune-checkpoint proteins such as programmed cell death protein 1 (PD-1), have achieved clinical success in the management of various cancers (Sharma and Allison, 2015). The high tumor mutation burden in SCLC provides a rationale for investigating the effect of immune-checkpoint blockades (ICBs) in this tumor type (Alexandrov et al., 2013; George et al., 2015; Hellmann et al., 2018). Indeed, results from a phase 3 trial led to Food and Drug Administration (FDA) approval of atezolizumab (anti-PD-L1) in combination with carboplatin and etoposide for the first-line treatment of patients with extensive stage (ES)-SCLC, despite achieving only a 2-month increase in overall survival (OS) (Horn et al., 2018). However, a large number of patients do not respond to ICBs. This highlights the need to identify new combination regimens to trigger anti-tumor immunity.

CDK7 is a master regulator of cell-cycle progression (Fisher and Morgan, 1994; Ganuza et al., 2012). CDK7 functions as the catalytic core of the CDK-activating kinase (CAK) complex and becomes activated by binding to Cyclin H and Mat1 (Harper and Elledge, 1998; Schachter and Fisher, 2013). The trimeric CAK complex activates several central cell-cycle CDKs by phosphorylation (Larochelle et al., 2007; Merrick et al., 2008; Schachter et al., 2013). Temporal activation of these CDKs by the CAK complex ensures orderly progression within the cell cycle (Asghar et al., 2015). In addition, CAK is a component of the general transcription factor TFIIH, a protein complex important for RNA polymerase II (RNA Pol II)-mediated transcription (Glover-Cutter et al., 2009; Larochelle et al., 2012; Serizawa et al., 1995; Shiekhattar et al., 1995). However, whether CDK7 kinase activity is indispensable for basal transcription remains controversial (Ganuza et al., 2012; Kanin et al., 2007; Serizawa et al., 1993). We previously reported that SCLCs are sensitive to THZ1, a covalent inhibitor of CDK7 that also targets CDK12/13. Due to this dual specificity of THZ1, it was challenging to pinpoint the distinct role of CDK7 in regulating transcription and cell-cycle progression, respectively (Christensen et al., 2014). We have recently identified a new highly selective covalent CDK7 inhibitor, YKL-5-124, with no off-target effect on CDK12/13 (Olson et al., 2019). The discovery of YKL-5-124 confirmed the role of CDK7 in regulating cell-cycle progression and suggested potential redundancies in its control of gene transcription.

While previous work has elucidated CDK7 as a master regulator of the cell cycle, its potential effects on DNA replication and genome stability, as well as its tumor-intrinsic immune

effect, remain unknown. Using YKL-5-124, we studied the effect of CDK7 inhibition in triggering an immune response and explored the efficacy of combining YKL-5-124 with immunotherapy in mouse models.

RESULTS

YKL-5-124 Specifically Targets CDK7 and Disrupts Cell-Cycle Progression through Inhibition of CDK7 CAK Activity

To confirm that YKL-5-124 confers selective engagement of CDK7 over CDK12/13 in SCLC cells, we performed a competitive pull-down assay and examined the ability of YKL-5-124 to block the pull-down of CDK7-Cyclin H complexes or Cyclin K, the obligate binding partner of CDK12/13 (Kwiatkowski et al., 2014). YKL-5-124 efficiently prevented Cyclin H pull-down but failed to block pull-down of Cyclin K (Figures 1A and S1A). These results confirm selective targeting of CDK7 by YKL-5-124, consistent with our recent findings in other cellular models (Olson et al., 2019).

We next examined direct targets of CDK7, CDK1, and CDK2. YKL-5-124 robustly inhibited CDK1 and CDK2 T-loop phosphorylation in a representative panel of SCLC lines at concentrations as low as 50 nM (Figures 1B and S1B). In contrast, YKL-5-124 treatment had no effect on C-terminal domain (CTD) phosphorylation of RNA Pol II (Figure 1B), indicating that selective CDK7 inhibition does not inhibit global transcription. We further confirmed that dual inhibition of CDK7 and CDK12/13 is required for inhibition of RNA Pol II CTD phosphorylation by co-treating cells with YKL-5-124 and the CDK12/13 inhibitor THZ531 (Zhang et al., 2016). Concurrent inhibition of CDK7 and CDK12/13 reduced levels of phosphorylated Pol II Ser2 and Ser5 to levels similar to treatment with the CDK7/12/13 inhibitor THZ1 (Kwiatkowski et al., 2014) (Figure S1C). In summary, selective CDK7 inhibition with YKL-5-124 is sufficient to reduce the phosphorylation levels of CDK1 and CDK2 but not that of RNA Pol II CTD. Furthermore, YKL-5-124 treatment had no effect on expression of superenhancer (SE)-associated genes including *INSM1*, *ASCL1*, *NFIB*, and *MYC* (Christensen et al., 2014), while THZ1 treatment caused a significant reduction in their expression (Figure S1D).

We next investigated whether YKL-5-124 treatment affected cell viability and cell-cycle progression. We first measured cell viability at different time points (up to 7 days) upon treatment with increasing concentrations of YKL-5-124. A significant reduction in growth rate was observed at all tested concentrations compared with control cells (Figures 1C and S1E). YKL-5-124 resulted in reduced growth and a cytostatic effect with a tendency of cytotoxic effects at longer time points (day 7) (Figures 1C and S1E). Cell-cycle analysis further showed that YKL-5-124 induced a significant accumulation of cells in G₁ phase with a corresponding loss of cells in S phase (Figures 1D and S1F). The percentage of cells in G₂/M phase was not significantly changed at concentrations up to 500 nM. In parallel, an increase of Cyclin E protein and mRNA (*CCNE1*) levels was detected, supporting the observed accumulation of cells at the G₁-S phase checkpoint, whereas expression of Cyclins A (*CCNA1*), B (*CCNB1*), and D (*CCND1*) remained unchanged (Figures 1E and 1F).

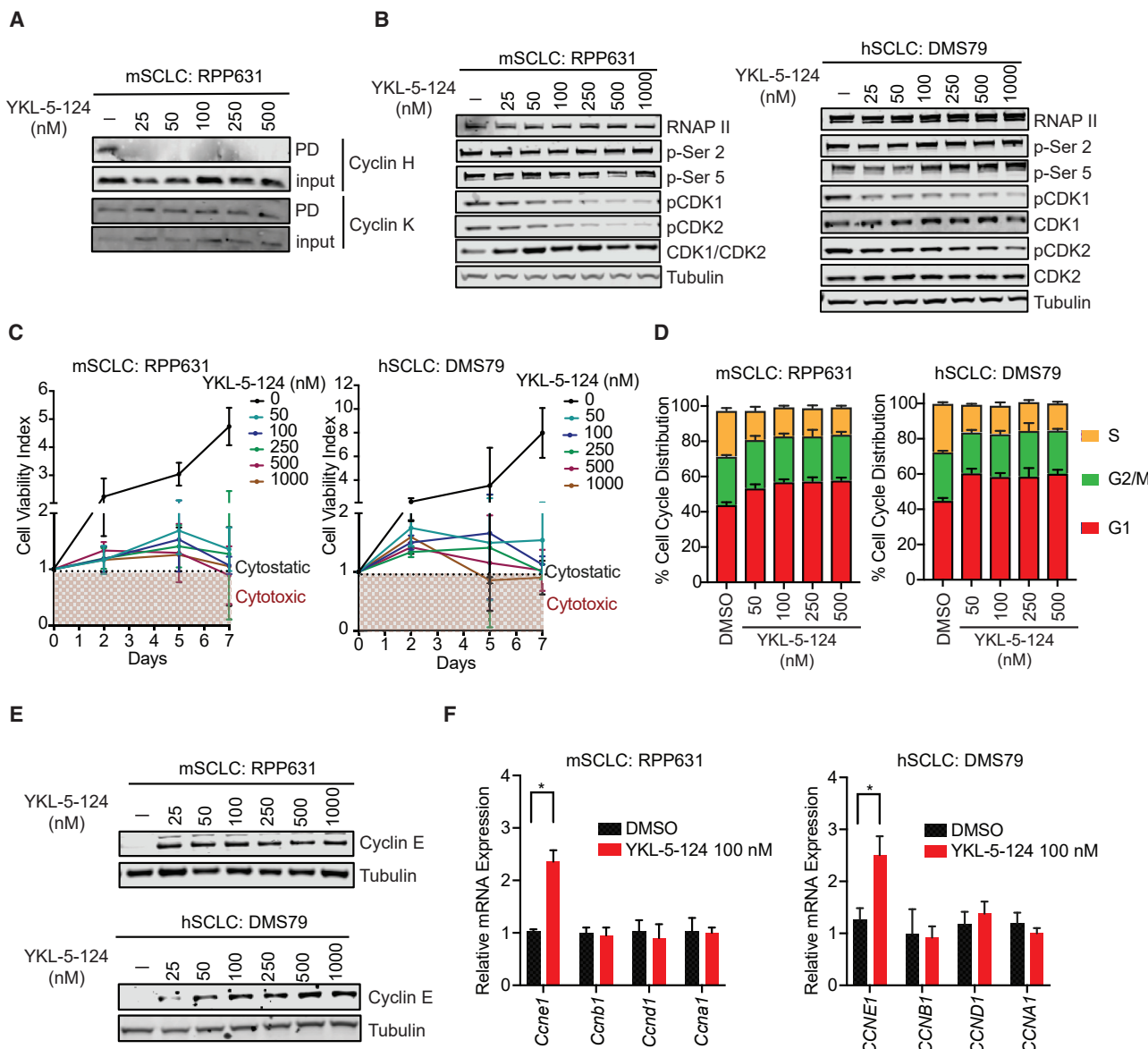


Figure 1. YKL-5-124 Specifically Targets CDK7 and Disrupts Cell-Cycle Progression through Inhibition of CDK7 CAK Activity

(A) Competitive pull-down assay in mouse SCLC (mSCLC) RPP631 cells treated with YKL-5-124 at indicated concentrations for 6 h. Western blotting showing the pull-down (PD) or input of Cyclin H and Cyclin K.

(B) Western blotting of RNA Pol II total (RNAP II), RNA Pol II p-Ser 2 and 5, CDK1, CDK2, pCDK1 (Thr161), pCDK2 (Thr160), and Tubulin in RPP631 and human SCLC (hSCLC) DMS79 cells after treatment with YKL-5-124 at indicated concentrations for 24 h.

(C) Cell viability was measured at day 2, 5 and 7 (and normalized to day 0) upon treatment with DMSO or indicated concentrations of YKL-5-124 in RPP631 and DMS79.

(D) Bar graph showing the cell distribution in G₁, S, and G₂/M phases quantified by flow-cytometry analysis of propidium iodide (PI) staining in RPP631 and DMS79 after YKL-5-124 treatment for 72 h.

(E) Western blotting analysis of Cyclin E and Tubulin levels in RPP631 and DMS79 after treatment with YKL-5-124 at indicated concentrations for 24 h.

(F) qRT-PCR analysis of CCNE1, CCNB1, CCND1, and CCNA1 gene expression in RPP631 and DMS79 after treatment for 24 h. The data are presented as fold changes compared with the vehicle (DMSO). *p < 0.05 (unpaired two-tailed t test).

In (C), (D), and (F), data shown as means ± SD in one of three independent experiments run in triplicates. See also Figure S1.

Consistent with recent findings in other models (Olson et al., 2019), our data in SCLC further support YKL-5-124 as a selective CDK7 inhibitor that suppresses CDK1 and CDK2 activity and impairs cell growth and cell-cycle progression.

CDK7 Inhibition Impairs DNA Replication and Causes DNA Damage and Micronuclei Formation

The inhibitory effect of YKL-5-124 on CDK1 and CDK2 activity and the consequent G₁-S progression defect prompted us to

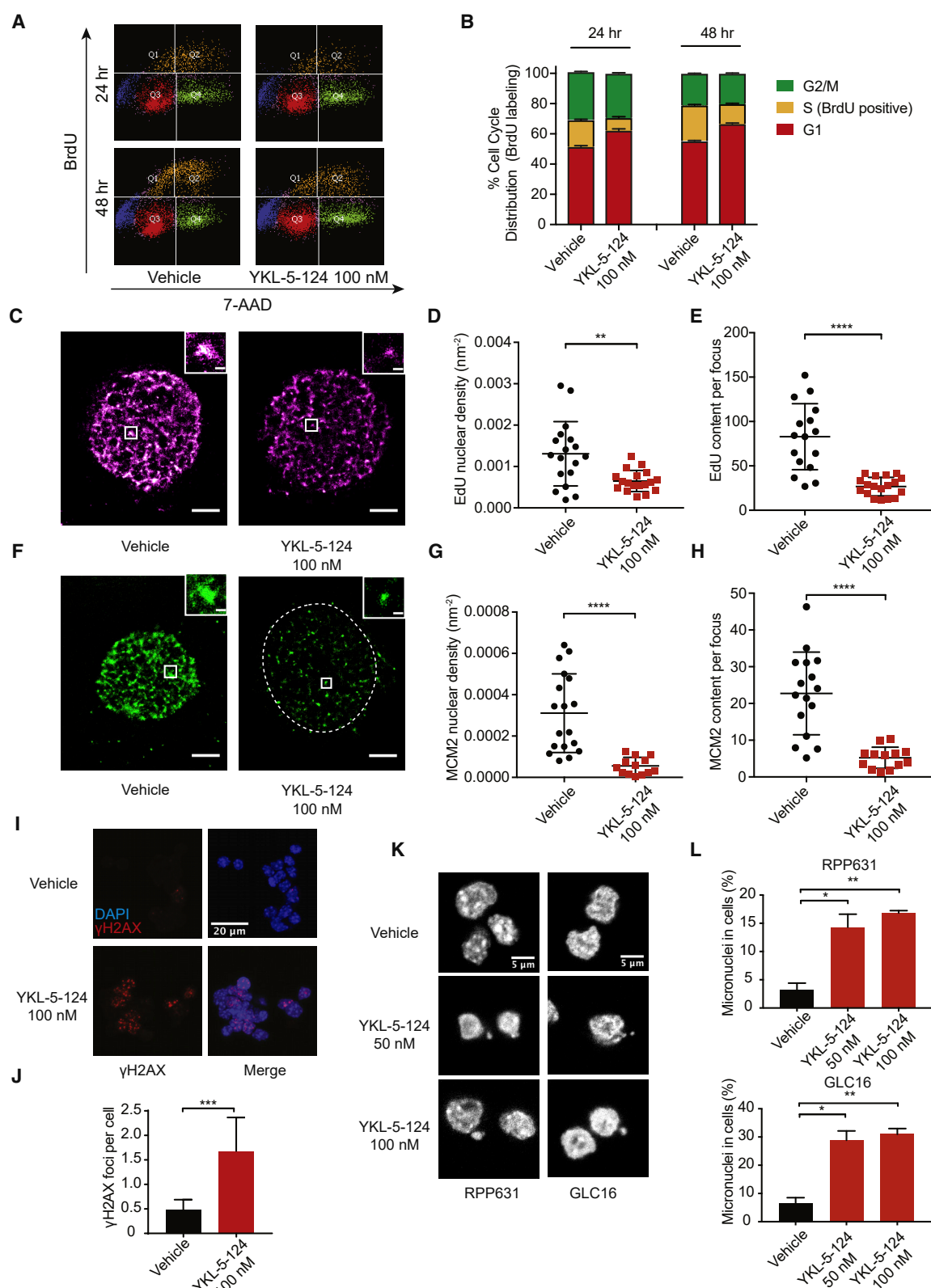


Figure 2. CDK7 Inhibition Impairs DNA Synthesis and MCM2 Complex and Causes DNA Damage and Micronuclei Formation

(A) Flow-cytometry analysis of BrdU and 7-AAD co-staining in DMS79 after 24 and 48 h treatment with DMSO or 100 nM YKL-5-124.
(B) Bar graph showing the cell distribution in G₁, S, and G₂/M phases.

(legend continued on next page)

address whether CDK7 inhibition affects DNA replication and hexameric minichromosome maintenance 2–7 (MCMs) (Hills and Diffley, 2014; Hyrien, 2016) complex at replication sites, subsequently causing DNA damage and genome instability.

We first examined the effect of YKL-5-124 on active DNA replication by measuring bromodeoxyuridine (BrdU) incorporation. A significant decrease in BrdU-incorporated S-phase cells was revealed (Figures 2A and 2B), indicating impaired DNA replication. We then sought to further characterize whether YKL-5-124 stalls DNA synthesis indicated by 5-ethynyl-2'-deoxyuridine (EdU) incorporation in the nucleus, as well as impairs the loading of MCM2 at individual replication foci. We employed single-molecule STORM (stochastic optical reconstruction microscopy) of fluorescently labeled EdU and MCM2 (Rust et al., 2006). We observed a dramatic decrease in the EdU content in each nucleus as well as in each focus upon YKL-5-124 exposure after 48 and 72 h (Figures 2C–2E, S1G, and S1H), implying reduced origin firing events. Similarly, a significant decline of MCM2 content in each nucleus and replication focus was detected (Figures 2F–2H, S1I, and S1J). Taken together, these results support an inhibitory impact of YKL-5-124 on DNA replication and MCM2 initiation complex assembly.

Reduction of MCM2 at the DNA replication initiation complex has been shown to cause replication deficiency and stress, leading to DNA damage and genomic instability, manifested by elevated levels of γH2AX and increased micronuclei formation. We observed a significant increase of γH2AX foci in YKL-5-124-treated cells after 48 h (Figures 2I and 2J), suggesting activation of the DNA-damage response. We then examined whether CDK7 inhibition can increase micronuclei. Immunofluorescence images of 4',6-diamidino-2-phenylindole (DAPI)-stained nuclei were recorded and quantified (Figure 2K). Percentages of cells containing micronuclei were considerably increased after YKL-5-124 treatment (Figure 2L).

YKL-5-124 Triggers Immune-Response Signaling and Induces Pro-inflammatory Cytokines/Chemokines Production

A growing body of evidence demonstrates that increased formation of micronuclei links genome instability to immunity (Bakhoun and Cantley, 2018; Mackenzie et al., 2017). We next performed transcriptomic analysis to comprehensively explore whether CDK7 inhibition affects immune-response signaling *in vitro*. RPP631 cells were treated with YKL-5-124 for 48 h and were then harvested for RNA sequencing. As expected, expression analysis across significantly modulated genes revealed that YKL-5-124 downregulated genes within gene set

enrichment analysis (GSEA) terms associated with cell cycle, mitosis, and E2F targets (Figures S2A–S2D). Our analysis further confirmed that YKL-5-124 treatment had little effect on expression of SCLC SE-associated genes, in comparison with dual CDK7 and CDK12/13 inhibition upon THZ1 treatment (Christensen et al., 2014) (Figures S2E and S2F). Intriguingly, GSEA of the differentially expressed genes revealed that three of the top five most positively regulated “hallmark” signatures were “Interferon-γ (IFN-γ) response” (Figure 3A), “Tumor necrosis factor α (TNF-α) signaling” (Figure 3B), and ‘Inflammatory response’ (Figure 3C).

Heatmaps for the most differentially regulated genes in the top GSEA signatures induced by YKL-5-124 showed an increased expression of numerous central pro-inflammatory cytokines and chemokines, including TNF-α pathway components and C-X-C motif chemokine ligand 10 (Cxcl10) (Figures 3D–3F). TNF-α signaling plays an important role in dendritic cell recruitment, maturation, and activation (Brunner et al., 2000), while CXCL10/CXCL9 are involved in regulating T cell recruitment and activity (Spranger et al., 2017). These factors secreted in the tumor microenvironment (TME) can potentially contribute to an optimal anti-tumor T cell response. We then sought to measure the expression levels of *Tnf*, *Cxcl10*, and *Cxcl9* upon YKL-5-124 exposure by quantitative reverse transcription-polymerase chain reaction (qRT-PCR). YKL-5-124 significantly stimulated tumor cell expression of *Tnf* (Figure 3G), *Cxcl10* (Figure 3H), and *Cxcl9* (Figure 3I) after 48 h. To further confirm that the cytokine/chemokine production by YKL-5-124 is mediated through specific inhibition of CDK7, we used an isogenic HAP1 cell system expressing CDK7 wild type (WT) or a mutated form of CDK7 (CDK7-Cys312Ser) in which YKL-5-124 cannot bind (Olson et al., 2019). Consistently, a significant increase in *TNF* and *CXCL10* expression was detected after YKL-5-124 treatment in the WT cells but not in the C312S mutant cells (Figure S2G). In addition, the cGAS-STING pathway is one of the most investigated cytosolic DNA-sensing mechanisms that activate immunity (Bakhoun and Cantley, 2018; Mackenzie et al., 2017). However, interestingly, the immune-stimulatory effect by YKL-5-124 appears to be independent of this pathway (Figures S2H and S2I).

We next sought to examine whether this tumor-cell-intrinsic effect by YKL-5-124 could affect T cell activation *ex vivo*. To address this, we utilized the OT-I mouse model in which the OT-I CD8⁺ T cells can recognize ovalbumin peptide residues 257–264 (OVA_{257–264}) and become activated (Barilla et al., 2019; Hogquist et al., 1994). Mouse SCLC cells were treated with either dimethyl sulfoxide (DMSO) or YKL-5-124 for 48 h. DMSO-conditioned or YKL-5-124-conditioned medium was

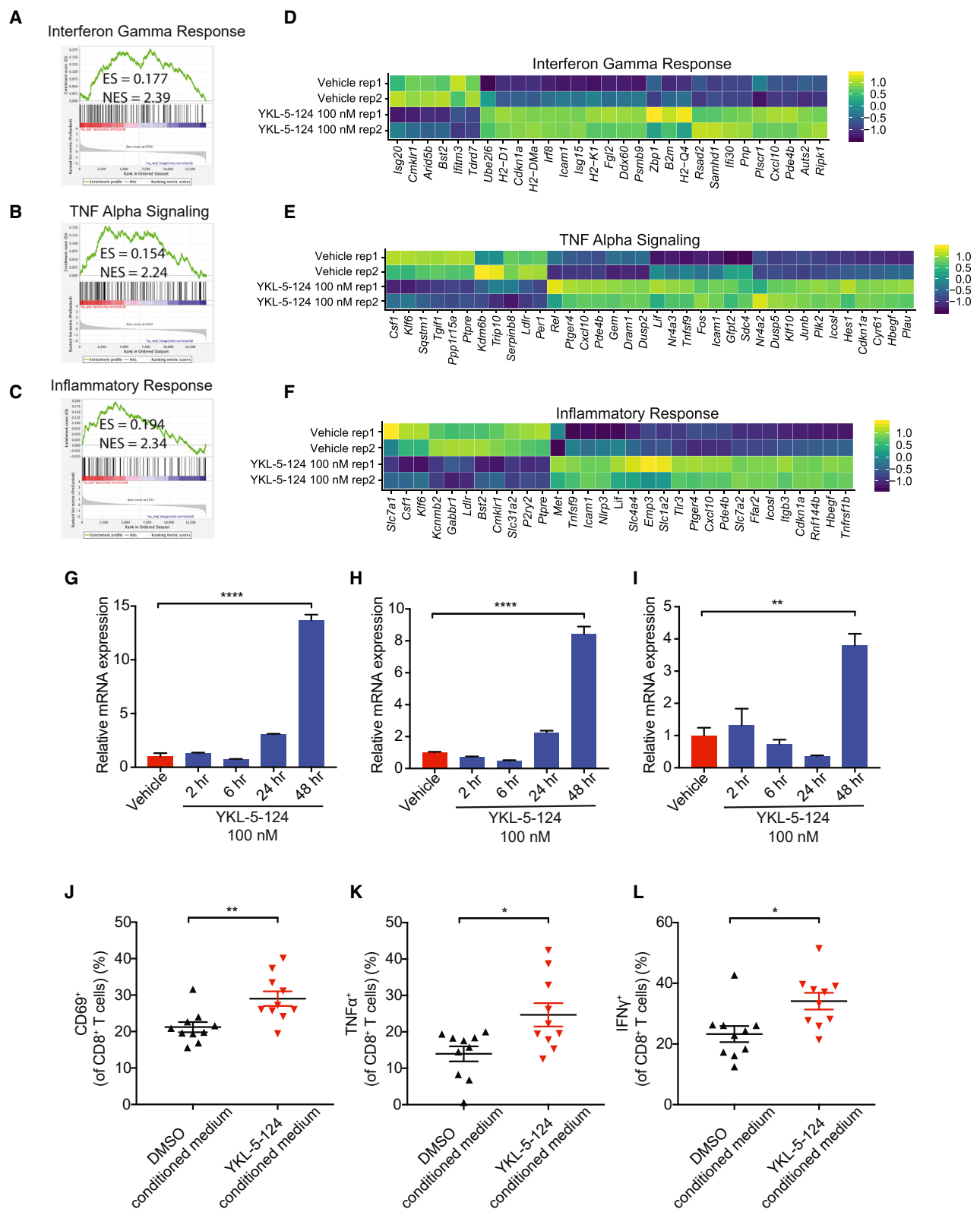
(C–E) Quantification of DNA synthesis indicated by EdU incorporation per nucleus as well as within each replication focus using STORM imaging of fluorescently labeled EdU in RPP631 cells treated with vehicle or 100 nM YKL-5-124 after 72 h. (C) Representative images of nuclei with EdU signal are shown in vehicle or YKL-5-124. Scale bars, 2,000 nm. (D) Quantifications of EdU nuclear density (nm^{-2}) per nucleus and (E) EdU content per focus are plotted.

(F–H) Quantification of MCM2 complex per nucleus as well as within each replication focus in RPP631 cells. (F) Representative images of nuclei with MCM2 content are shown. Scale bars, 2,000 nm. Dashed-line circle indicates nuclei. (G) Quantification of MCM2 nuclear density (nm^{-2}) per nucleus and (H) MCM2 content per focus are plotted.

(I and J) Quantification of γH2AX foci upon YKL-5-124 exposure by immunofluorescence (IF) microscopy in RPP631. (I) Representative images of DAPI-stained nuclei in blue and γH2AX foci in red. (J) The percentages of γH2AX foci in cells are plotted. At least ten field images were counted (≥ 100 cells).

(K and L) Quantification of micronuclei upon YKL-5-124 exposure in RPP631 and GLC16 by IF. (K) Representative images of DAPI-stained nuclei. (L) The percentages of micronuclei in cells are plotted. At least ten field images were counted (≥ 100 cells).

In (B), (D), (E), (G), (H), (J), and (L), data shown as means \pm SD in one of two to three independent experiments run in triplicates. In (D), (E), (G), (H), (J), and (L), *p < 0.05, **p < 0.01, ***p < 0.001, and ****p < 0.0001 (unpaired two-tailed t test). See also Figure S1.



(legend on next page)

added to OT-I T cell culture in the presence of OVA_{257–264} peptide. Intriguingly, a significant increase in the percentage of CD69⁺, TNF- α ⁺ and IFN- γ ⁺ CD8⁺ T cells was detected in the YKL-5-124-conditioned medium, in comparison with the DMSO-conditioned medium group (Figures 3J–3L), indicating elevated T cell activity. No significant effect on CD8⁺ T cell activity was observed when OT-I T cells were directly treated with YKL-5-124 (Figures S2J–S2L). These findings indicate that the activation of CD8⁺ T cells is a tumor-intrinsic effect of CDK7 inhibition rather than the drug's direct action on CD8⁺ T cells.

Collectively, these findings suggest that CDK7 inhibition activates immune-response signaling in SCLC cells, leading to secretion of essential pro-inflammatory cytokines/chemokines, which in turn can activate CD8⁺ T cells.

YKL-5-124 Is a Well-Tolerated CDK7 Inhibitor *In Vivo* and Inhibits SCLC Tumor Growth

We next determined whether YKL-5-124 might inhibit tumor growth and prolong survival in four immunocompetent murine SCLC models: *Rb1*^{L/L}*p53*^{L/L}*p130*^{L/L} (RPP) genetically engineered mouse models (GEMMs) (Schaffer et al., 2010), RPP, *Rb1*^{-/-}*p53*^{-/-} (RP), and RPP-MYC orthotopic models (Figures S3A and S3B).

To overcome the long and variable latency (6–9 months) of conventional RPP GEMMs, we established and characterized an orthotopic syngeneic SCLC model. This was conducted via transthoracic injection using tumor cells from a CRISPR/Cas9-RPP model of C57BL/6 (B6) background (Oser et al., 2019) (Figure S3C). These tumor-bearing mice have a much shorter and consistent latency of 7–8 weeks. Furthermore, a highly similar frequency of different immune infiltrating populations (CD3⁺, CD4⁺, CD8⁺, and CD11b⁺) in the TME between the orthotopic model and GEMMs was observed (Figures S4A–S4E). To this end, using the same strategy we successfully generated three syngeneic murine models (RPP, RP, and RPP-MYC), which are fast and reliable for oncoimmunology studies for SCLC (Figure S3).

To evaluate the optimal YKL-5-124 dosage with minimum toxicity, we performed a dose-escalating study in B6 mice in which body weight and blood cell counts were monitored and measured (Figures S5A–S5D). YKL-5-124 was well tolerated at a dose up to 10 mg/kg and caused no significant change in body weight and blood counts. We furthermore confirmed target engagement of YKL-5-124 in tumor-bearing mice at 10 mg/kg (Figure S5E).

We first tested whether YKL-5-124 affects tumor growth in the RPP orthotopic model. Disease development was followed by magnetic resonance imaging (MRI). Upon confirmation of tumor

burden by MRI, mice were randomized to control and YKL-5-124 treatment, respectively (Figure 4A). All mice in the control group displayed aggressive disease with tumor volumes doubling after a 3-week period (Figures 4B and 4C). YKL-5-124-treated mice had significant tumor response at the 2-week and 3-week time points (Figures 4B and 4C). We next examined the efficacy of YKL-5-124 in the RP and RPP-MYC orthotopic models (Figures 4D and S6A–S6D). Consistently, YKL-5-124 demonstrated notably delayed tumor growth in the RP and RPP-MYC (Figures 4E and S6A–S6D). Remarkably, YKL-5-124 significantly prolonged survival, with an added median survival benefit of approximately 30 days in both RPP and RP models (Figures 4F and 4G). In contrast, most vehicle-treated mice in the RPP model succumbed to their tumor burden before the 6-week time point, highlighting the aggressive disease course (Figure 4F).

To further confirm the above observed tumor response, we evaluated the efficacy of YKL-5-124 in autochthonous RPP GEMMs (Figures S6E–S6H). Consistently, the majority of mice in control group (seven of eight) had doubled their tumor volumes at the 3-week time point, while none of the mice treated with YKL-5-124 had more than 50% increase of tumor burden (Figures S6F and S6G). Similarly, YKL-5-124 greatly improved median OS from 28 days to 56 days (Figure S6H).

YKL-5-124 Enhances Tumor Response to Anti-PD-1 Immunotherapy

Our *in vitro* findings suggest a potential role of CDK7 inhibition in enhancing immune response. This prompted us to investigate whether CDK7 inhibition could augment immunotherapy *in vivo*. Thus, we next sought to explore whether combining YKL-5-124 with anti-PD-1 could result in more durable tumor inhibition than each single agent alone. Of note, no toxicity was detected in the body weight and blood cell counts in the combination treatment group (Figures S6I–S6L).

Compared with the control group, anti-PD-1 alone significantly reduced tumor growth after 3-week treatment in the RPP and RP models (Figures 4B and 4E), although to a lesser extent when compared with YKL-5-124, as the added median OS benefit by anti-PD-1 was only 10 days in the RPP and 15 days in the RP model (Figures 4F and 4G). Strikingly, mice in the combined anti-PD-1 + YKL-5-124 treatment regimen (Combo) had the best response across all models tested (Figures 4B, 4E, S6C, and S6F). We observed that 7 out of 25 mice exhibited stable disease (volume increase <30%) including three mice with complete response (CR) in the RPP model (Figure 4B), and more than half of the mice had stable disease with one CR in the RP model (Figure 4E). Most importantly, combining YKL-5-124 and anti-PD-1 dramatically increased the OS of

Figure 3. YKL-5-124 Triggers Immune-Response Signaling and Induces Pro-inflammatory Cytokine and Chemokine Production

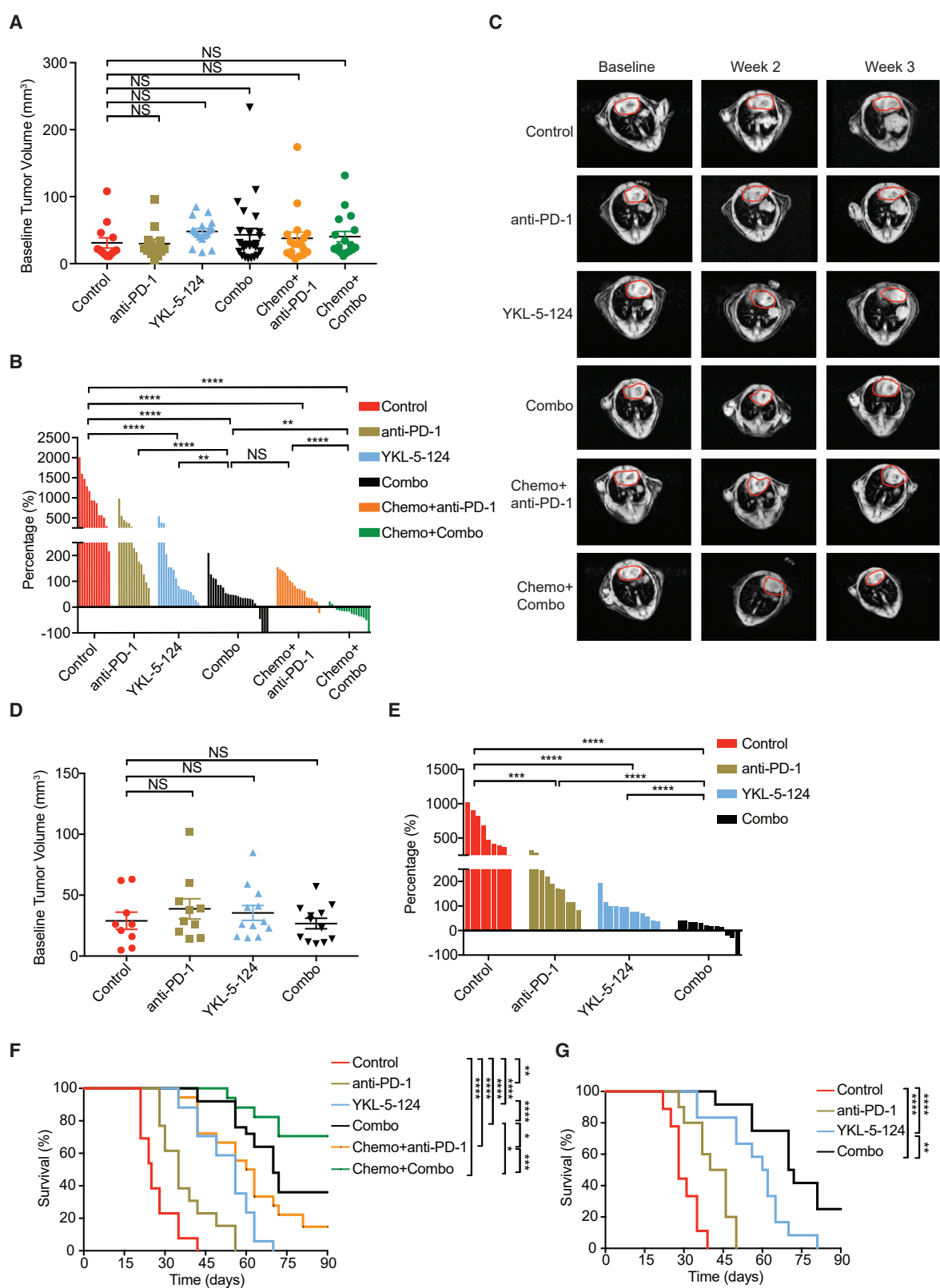
(A–C) GSEA of the differentially expressed genes induced by YKL-5-124 in RPP631. Shown are three of the top five most positively regulated “hallmark” signatures: (A) interferon- γ response, (B) TNF- α signaling, and (C) inflammatory response. Gene list was ranked with signed (from \log_2 fold change [\log_2 FC]) likelihood ratio from YKL-5-124 versus vehicle comparison.

(D–F) Heatmaps for differential expression of transcripts from three top positively regulated pathways (colors are \log_2 FC).

(G–I) qRT-PCR analysis of (G) *Tnf*, (H) *Cxcl10*, and (I) *Cxcl9* levels in RPP631. The data are presented as fold changes compared with the vehicle. Data shown as means \pm SD in one of three independent experiments run in triplicates. ** p < 0.01, *** p < 0.0001 (unpaired two-tailed t test).

(J–L) Profiling of OT-I T cells activation markers (J) CD69, (K) TNF- α , and (L) IFN- γ by flow cytometry after treatment with DMSO- or YKL-5-124-conditioned medium. Data shown as means \pm SEM in one of three independent experiments run in ten replicates. * p < 0.05, ** p < 0.01 (unpaired two-tailed t test).

See also Figure S2.



(legend on next page)

tumor-bearing mice in comparison with either YKL-5-124 or anti-PD-1 alone (Figure 4F). In comparison with control mice, combination treatment led to a more than 2-fold increase in survival with an added median survival benefit of 45 days and 43 days in the RPP and RP models, respectively (Figures 4F and 4G). These results were also confirmed in a separate cohort of RPP GEMMs. Whereas mice treated with anti-PD-1 alone had slower tumor growth compared with vehicle-treated mice after 3 weeks, the majority of YKL-5-124 plus anti-PD-1 treated mice (seven of nine) had substantially reduced tumor burdens (Figures S6F and S6G). Combination treatment was superior to either YKL-5-124 or anti-PD-1 alone in tumor response (Figures S6F and S6G) and led to the longest survival (Figure S6H).

We next sought to evaluate the efficacy of Combo with standard chemotherapy (cisplatin + etoposide) and compare the survival benefit with recently approved chemotherapy + anti-PD-1 (Horn et al., 2018). Strikingly, the four-drug combination group (Chemo + Combo) had the best efficacy (Figure 4B) with no toxicity in the body weight (Figure S6I). All mice had stable disease and roughly half of the 17 mice had >20% reduction in tumor volume after 3 weeks, whereas there was no significant difference in efficacy between YKL-5-124 + anti-PD-1 (Combo, Figure 4B) and cisplatin + etoposide (Chemo + anti-PD-1, Figure 4B). The impressive efficacy of Chemo + Combo was directly translated into the longest improved survival, as 12 out of 17 mice in this group survived more than 90 days (Figure 4F). Of note, mice under Combo treatment appear to live significantly longer than those in the Chemo + anti-PD-1 group (Figure 4F), suggesting a better survival benefit in the Combo group.

In summary, YKL-5-124 enhances the response to anti-PD-1 immunotherapy, and combining YKL-5-124 with anti-PD-1 offers significant survival benefit in multiple murine models. Adding YKL-5-124 and anti-PD-1 to standard chemotherapy further improves tumor response and leads to the longest survival.

YKL-5-124 Provokes a Robust Anti-tumor Immune Program *In Vivo*, Which Is Further Enhanced by Anti-PD-1 Immunotherapy

The survival benefit from combining YKL-5-124 and anti-PD1 treatment suggested that combined CDK7 and PD-1 inhibition might further alter the tumor immune milieu to achieve optimal immune response.

To investigate the phenotypical and functional alterations of T cells, we harvested mouse tumor-bearing lung for immune

profiling after 7-day treatment, as shown in Figure S4A. There was no significant change of the frequencies of total CD4⁺ and CD8⁺ T cell infiltrates after either anti-PD-1 or YKL-5-124 compared with control tumors (Figures 5A and 5B). However, a notable increase of total CD4⁺ T cell infiltrates was observed in the combination-treated mice in comparison with control tumors or those treated with YKL-5-124 alone, and this trend was not seen in total CD8⁺ T cells (Figures 5A and 5B). Profiling of CD4⁺ T cells showed a substantial increase of CD44^{high}CD62L^{low} effector CD4⁺ T cells after either YKL-5-124 or anti-PD-1 treatment (Figures 5C and 5D), while combination treatment induced the highest increase of CD44^{high}CD62L^{low} CD4⁺ T cells (Figures 5C and 5D), which was further confirmed in a separate cohort of RPP GEMMs (Figures S6M and S6N).

To further assess the functional activity of CD4⁺ T cells, we analyzed the expression of a proliferation marker, Ki67, and an activation/co-stimulatory marker, ICOS. YKL-5-124 led to a modest increase of tumor-infiltrating CD4⁺ T cells expressing Ki67, and significantly higher frequencies of ICOS⁺ CD4⁺ T cells (Figures 5E and 5F). Anti-PD-1 also caused a moderate elevation of Ki67⁺ CD4⁺ T cells but had no effect on the levels of ICOS⁺ CD4⁺ T cells (Figures 5E and 5F), suggesting that YKL-5-124 might be more effective than anti-PD-1 in promoting activation of CD4⁺ T cells. The most marked increase of Ki67⁺ CD4⁺ (Figure 5E) and ICOS⁺ CD4⁺ T cells (Figures 5F and S6O) was detected in mice treated with the YKL-5-124 and anti-PD-1 combination. We next assessed the activity of cytotoxic T lymphocytes (CTLs) by staining for Granzyme B (GzmB), a cytotoxic granule protein secreted by CD8⁺ T cells. A considerable but equivalent increase of GzmB⁺ CD8⁺ T cell percentage was observed in YKL-5-124 or anti-PD-1-treated mice (Figure 5G), suggesting an enhanced cytotoxic T cell-mediated clearance of tumor cells. Of note, combination treatment resulted in the highest percentage of GzmB⁺ CD8⁺ cytotoxic T cells (Figures 5G and S6P), supporting the superior efficacy and improved survival induced by YKL-5-124 and anti-PD-1.

An optimal and efficient anti-tumor immune program requires cooperation between dendritic cells (DCs) and T cells. CD4⁺ T cells provide the key input signals for the DCs to relay the help signal to elicit CD8⁺ CTLs responses (reviewed in Borst et al., 2018). In particular, recent work highlighted the critical role of CD11c⁺ CD103⁺ DCs in the priming and effector phase of the anti-tumor T cell response (Salmon et al., 2016; Spranger et al., 2017). We sought to characterize whether YKL-5-124 and

Figure 4. YKL-5-124 Inhibits SCLC Tumor Growth *In Vivo* and Enhances Tumor Response to Anti-PD-1 Immunotherapy

- (A) Quantification of baseline tumor volumes of RPP orthotopic model. Combined vehicle and isotype immunoglobulin G (Control, n = 13), anti-PD-1 (n = 13), YKL-5-124 (n = 17), anti-PD-1 + YKL-5-124 (Combo, n = 25), chemotherapy (Chemo) + anti-PD-1 (n = 18), and Chem + Combo (n = 17). Each dot represents one mouse.
- (B) Quantification of tumor volume changes of RPP orthotopic model after treatment. Waterfall plot shows tumor volume response after week 3. Each column represents one mouse, in comparison with baseline MRI measurement.
- (C) Representative MR images show lung tumors of RPP orthotopic model before and after the treatment at indicated time points. Circled areas, heart.
- (D) Quantification of baseline tumor volumes of RP orthotopic model: Control (n = 9), anti-PD-1 (n = 10), YKL-5-124 (n = 12), and Combo (n = 12). Each dot represents one mouse.
- (E) Quantification of tumor volume changes of RP orthotopic model after treatment. Waterfall plot shows tumor volume response after week 2. Each column represents one mouse, in comparison with baseline MRI measurement.
- (F and G) Kaplan-Meier survival curve of (F) RPP or (G) RP orthotopic model after indicated treatment. *p < 0.05, **p < 0.01, ***p < 0.001, ****p < 0.0001 (log-rank test).
- In (A) and (D), data shown as means ± SEM. In (A), (B), (D), and (E), **p < 0.01, ***p < 0.001, and ****p < 0.0001; NS, not significant (unpaired two-tailed t test). See also Figures S3–S6.

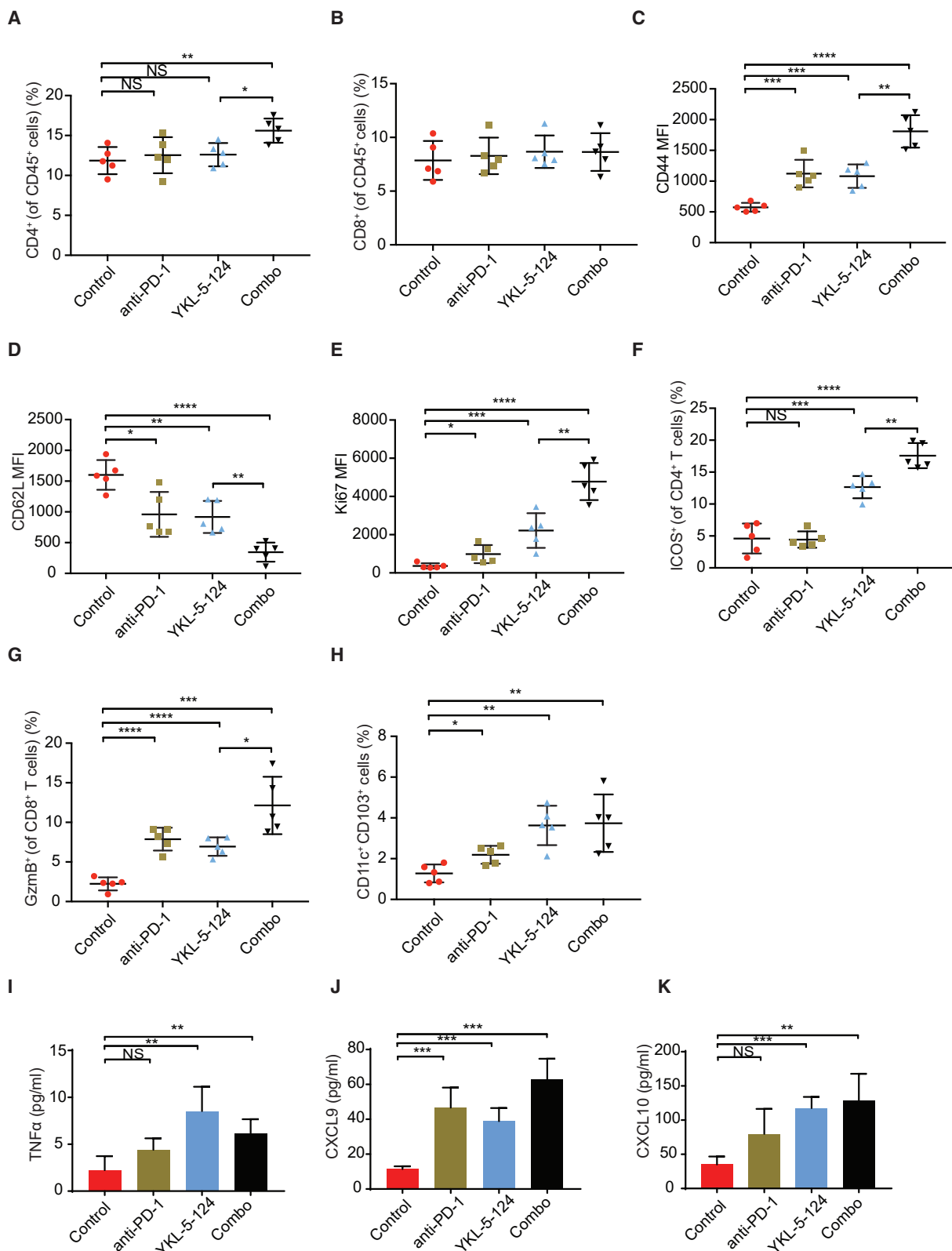


Figure 5. YKL-5-124 Provokes a Robust Anti-tumor Immune Program, Which Is Further Enhanced by Anti-PD-1 Immunotherapy

(A and B) Tumor-infiltrating lymphocytes from RPP orthotopic model were analyzed at day 7 after treatment ($n = 5$). Frequencies of infiltrating (A) CD4⁺ T cells and (B) CD8⁺ T cells are presented.

(legend continued on next page)

anti-PD-1 alone or combination treatment would have an impact on the DC population ($\text{MHCII}^+ \text{CD11c}^+ \text{CD103}^+$). Compared with control mice, a significant increase in percentages of tumor resident DCs was observed in mice after treatment with YKL-5-124 or combination, but to a lesser extent in mice treated with anti-PD-1 (Figure 5H). In addition, to directly examine the *in vivo* secretion of TNF- α , CXCL9, and CXCL10 in the TME, we collected bronchoalveolar lavage fluid (BALF) from mouse lung after 7 days of treatment. Consistent with our *in vitro* data, a pronounced increase of TNF- α , CXCL9, and CXCL10 was detected upon YKL-5-124 and combination treatment (Figures 5I–5K).

These findings suggest YKL-5-124 provokes a robust anti-tumor immune program elicited by cooperation between DCs, effector CD4 $^+$ T cells and cytotoxic CD8 $^+$ T cells. This effect is further enhanced by the addition of PD-1 blockade.

Single-Cell Transcriptomic Analysis Identifies Intratumoral Cell Populations

To provide a more comprehensive and unbiased assessment of immunotherapeutic responses, we performed single-cell RNA sequencing (scRNA-seq) analysis on the whole TME including tumor cells and immune counterparts.

We obtained single-cell transcriptomes for 9,307 cells in the control group, 10,018 in YKL-5-124, 5,944 in anti-PD-1, and 5,911 in Combo. To define the intratumoral cell populations, we computationally combined data from the four treatment groups using canonical correlation analysis (Butler et al., 2018), representing a total of 31,180 cells, then used graph-based clustering and dimensionality reduction with UMAP (Becht et al., 2018) to respectively identify and visualize transcriptionally homogeneous clusters of cells (Figure 6A). Clusters were further annotated by directly comparing their transcriptional state with that of known sorted populations using the SingleR package (Aran et al., 2019) and assessment of known cell-type specific markers. We identified cancer cells expressing the epithelial cell adhesion molecule (*Epcam*), lymphoid populations represented by T cells and innate lymphoid cells (ILC) expressing *Cd3d*, natural killer (NK) cells expressing natural cytotoxicity triggering receptor 1 (*Ncr1*), B cells expressing *Cd19*, and myeloid populations such as monocytes, DCs and macrophages, neutrophils expressing *S100a9*, basophils expressing *Cd200r3*, and stromal cells expressing *Sparc* (Figures 6A–6C and S7A). Notably, compared with distribution of cell populations in the control group, YKL-5-124, anti-PD-1, and Combo treatment resulted in an increase in the frequencies of total immune cell components (Figures 6D and 6E).

Single-Cell Transcriptomic Analysis Confirms Connection of CDK7 Inhibition in Tumor-Intrinsic Signaling to Immunity

As shown above, CDK7 inhibition impedes cell-cycle progression and DNA replication, leading to genome instability and

elevated immune response. To further delineate the temporal events that occur upon *in vivo* treatment, we inferred a continuous cell-cycle trajectory from the scRNA-seq data. First, we calculated scores for genes specific to the G₁, G₂/M, or S phase for each cell and applied the scores to cluster cells in eight groups that represent a cell-cycle state. The center of each group was then connected with its two nearest neighbors in the computed 3-dimensional (3D) cell-cycle score space (Figure S7B). The 3D visualization was projected in 2D by retaining the order of the eight cell-cycle states, which provides a portrait of the dynamic phases of cell-cycle progression (Figure 6F). Analysis of cell distribution illustrated that cells mainly arrested at G₁ phase (cluster 1) and to a lesser extent at G₂/M (cluster 8) upon YKL-5-124 and combination treatment, whereas a significant decrease in percentage of S-phase cells (clusters 4, 5, and 6) was observed (Figure 6G). Furthermore, GSEA showed that YKL-5-124 significantly downregulated genes within the “cell-cycle” and “E2F target” signatures (Figure 6H). These data further support the proposal that cell-cycle progression is substantially disrupted *in vivo* by CDK7 inhibition. Finally, YKL-5-124 and combination treatment triggered robust immune-response signaling, particularly gene signatures related to “IFN- γ response” and “Inflammatory response” (Figures 6I and 6J).

Combinatorial Therapy Reinvigorates Anti-tumor Immunity

To delineate an overall immune landscape remodeling associated with treatment, we characterized the alterations of the sub-populations of the tumor-infiltrating immune cells (Figures 7A and 7B). In comparison with control, a significant increase in percentage of total T cells, NK cells, and ILC cells was observed upon YKL-5-124, anti-PD-1, and combination (Figure 7B). In the myeloid compartments, anti-PD-1 induced an increase of monocytes and macrophages, while YKL-5-124 treatment induced higher numbers of monocytes and neutrophils (Figure 7B). Of note, although DCs accounted for a small fraction of the overall population, YKL-5-124, anti-PD-1, and combination all induced an increase in DCs (Figure 7B).

Our *in vivo* immune profiling suggests that YKL-5-124 and combination therapy provoke a robust anti-tumor immune program centered on effector CD4 $^+$ T cells and CD8 $^+$ T cells. Consistently, scRNA-seq analysis showed a particularly prominent impact on T cells (Figure 7B). To more accurately dissect the T cell subpopulations, we separated T cells (6,698) and analyzed the data at higher granularity (Figure 7C). This approach yielded 11 distinct T cell subpopulations (c0 to c10) broadly defined by the distribution of classical marker genes, representing high plasticity and complexity (Figures 7C–7H). It was evident that YKL-5-124, anti-PD-1, and combination prompted changes in subpopulation proportions and their transcriptional profiles (Figures 7I–7M). Further characterization of

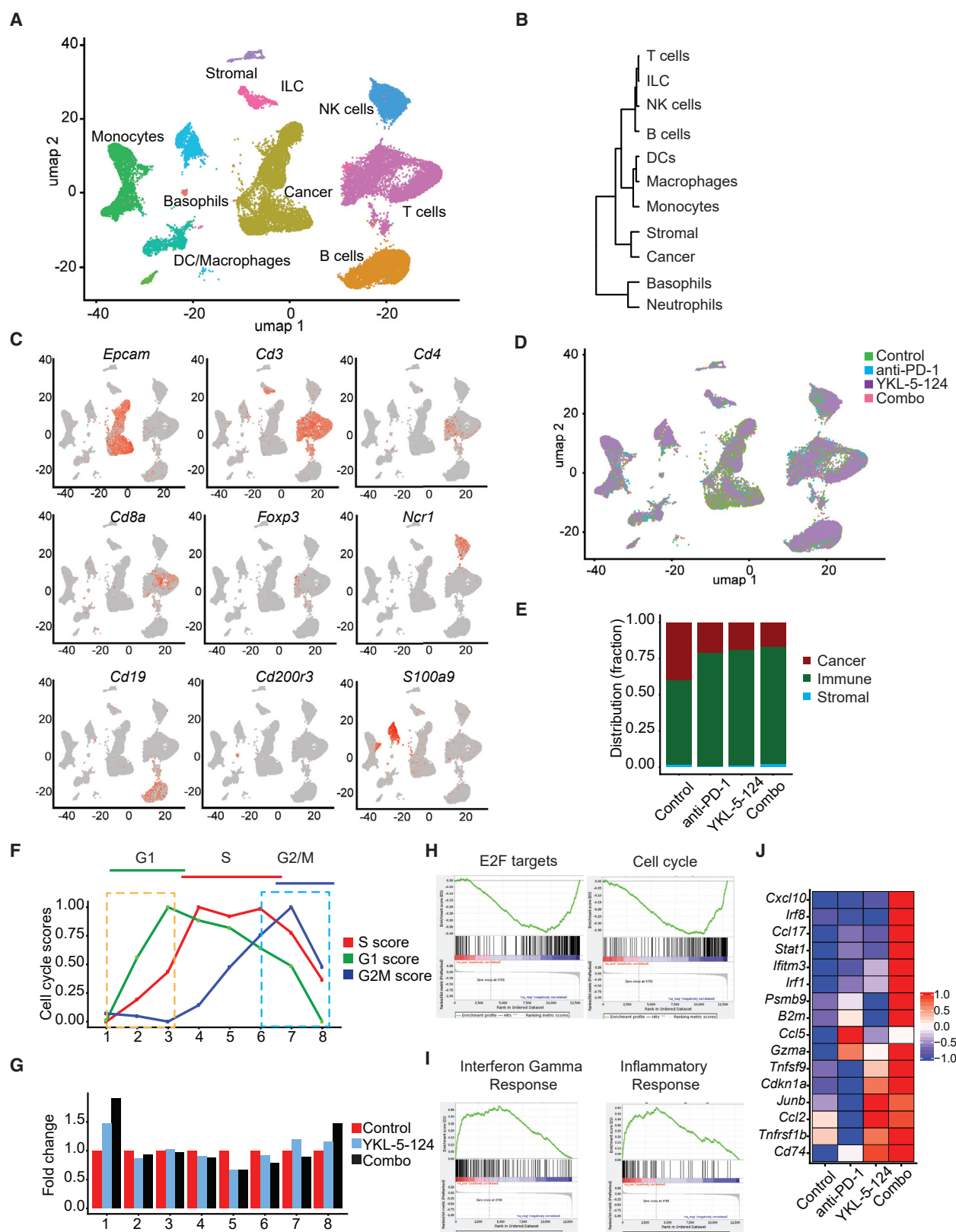
(C–F) The expression of (C) CD44, (D) CD62L, and (E) Ki67 in CD4 $^+$ T cells; (F) frequencies of ICOS $^+$ CD4 $^+$ T cells were analyzed ($n = 5$).

(G) Frequencies of Gzmb $^+$ CD8 $^+$ T cells were analyzed ($n = 5$).

(H) Frequencies of CD11c $^+$ CD103 $^+$ dendritic cells were analyzed ($n = 5$).

(I–K) Bronchoalveolar lavage fluid (BALF) was collected from mouse lung and secretion of (I) TNF- α , (J) CXCL9, and (K) CXCL10 was measured by Luminex (pg/mL) ($n = 4$).

Data shown as means \pm SD. * $p < 0.05$, ** $p < 0.01$, *** $p < 0.001$, **** $p < 0.0001$; NS, not significant (unpaired two-tailed t test). See also Figure S6.



(legend on next page)

each individual cluster is described here and detailed in **STAR Methods**.

CD4⁺ T Cells

Cells in c1 expressed high levels of Cd4 and the naive T cell marker *Sell* (CD62L), but lacked the expression of effector/memory marker *Cd44* and T cell activation genes (detailed in **STAR Methods**), including *Ifng* and *Icos* (Figure 7K). c1 appeared to be naive T cells, whose percentage was prominently reduced following YKL-5-124, anti-PD-1, and combination (Figures 7I and 7J). c5 showed the highest levels of activated markers and intermediate levels of *Sell* and *Cd44* (Figure 7K), representing an activated/effector T cell signature. c4 expressed much lower levels of these activation markers, and lower *Sell* and higher *Cd44* (Figure 7K). YKL-5-124, anti-PD-1, and combination treatment led to an increase in frequency of c5 and a slight reduction in c4 percentage (Figures 7I and 7J).

c6 cells expressed high levels of *Cd4* and *Foxp3*, which are markers for regulatory T cells (Tregs). Upon YKL-5-124, anti-PD-1, and combination treatment, the percentage of Tregs increased significantly in comparison with mice treated with control (Figures 7I and 7K). This increased frequency of Tregs might indicate an acute positive feedback to an activated tumor immune environment by short-term treatment.

c7 displayed highest levels of *Cd44* and low of *Sell*, and intermediate levels of T cell activation markers, indicating an effector/activation T cell signature. Of note, this cluster of cells expressed uniquely *Mki67*, implying proliferative capacity of these cells. In response to YKL-5-124, anti-PD-1, and combination treatment, the numbers of *Mki67*⁺ CD4⁺ T cells significantly increased (Figure 7J).

CD8⁺ T Cells

Both c0 and c8 expressed high levels of *Cd8a* and *Sell*, but low *Cd44* and T cell activation genes. c9 expressed intermediate level of *Sell* and relatively low level of T cell activation genes. Thus, c0, c8, and c9 appeared to be naive-like cells and in an inactivated state. Notably, YKL-5-124, anti-PD-1, and Combo all caused a reduction of these three clusters of CD8⁺ T cells (Figures 7I, 7L, and 7M).

c3 expressed high levels of memory T cell marker *Klrg1*, intermediate levels of cytotoxic T cells markers (*Gzma* and *Gzmb*), and *Tbx21* (T-bet) and *Eomes*. This cluster represents “memory” population with cytotoxicity and low-proliferation capability, which has the potential to differentiate into CTLs (Ebert et al., 2016; Herndler-Brandstetter et al., 2018). c10 showed the highest levels of T cell activation genes and *Gzma* and *Gzmb*, suggesting that these cells are fully differentiated CTLs. c5

expressed low levels of *Sell* but high *Cd44* and activation markers, representing an “effector” T cell signature (Figures 7I, 7L, and 7M). In comparison with control, proportions of cells in both c3 and c5 increased in all other groups, whereas the number of cells in c10 increased the most upon combination treatment (Figures 7I, 7L, and 7M). These findings suggest that combining YKL-5-124 and anti-PD-1 remodels the intratumoral CD8⁺ T cell population from cells that are more naive-like to those with more effector-like, activated, and cytotoxic properties.

In line with recent work (Gubin et al., 2018), our clustering also revealed that numerous clusters were categorized more based on their functional markers rather than classic cellular subtype. c7 cells with high levels of *Mki67* are composed of a mixture of CD4⁺ T cells and CD8⁺ T cells, highlighting their cell-proliferation capability (Figures 7E, 7F, 7H, 7K, and 7M). c5 is another functionally defined cluster of effector/activated T cells, which contain both CD4⁺ and CD8⁺ T cells (Figures 7E, 7F, 7H, 7K, and 7M). In response to YKL-5-124, anti-PD-1, and combination, the number of cells in c7 and c5 increased substantially (Figures 7J and 7L), implying a major impact on proliferation and activation of CD4⁺ and CD8⁺ T cells.

Collectively, our data highlight anti-tumor immunity alterations occurring in the intratumoral T cell compartment following YKL-5-124, anti-PD-1, and particularly combinational therapy, including: (1) a significant reduction in CD4⁺ and CD8⁺ naive T cell frequency; (2) a dramatic expansion of CD4⁺ and CD8⁺ effector/memory T cells and CD8⁺ CTLs, with an increase in the number of *Mki67*⁺ proliferating T cells; and (3) upregulation of an anti-tumor gene signatures of T cell activation/function.

Anti-tumor Immunity by Combining YKL-5-124 and PD-1 Is Partly Dependent on CD4⁺ and CD8⁺ T Cells

Our *in vivo* data demonstrate that combining YKL-5-124 and anti-PD-1 resulted in the best tumor response and optimal immune surveillance centered on T cells. To determine whether CD4⁺ or CD8⁺ T cells directly contribute to combination therapy response, we assessed the impact of perturbing immune cell function by *in vivo* neutralization antibodies against CD4 (α CD4) or CD8 (α CD8) (Figures S7C and S7D). Tumor-bearing mice were randomized to combination treatment or combination treatment plus α CD4 or α CD8. Indeed, compared with non-depletion mice in the combination group, CD4⁺ T cell-depleted mice had significantly higher tumor burdens (Figures 7N and 7O). Similarly, a dramatic increase of tumor volumes was observed in CD8⁺ T cell-ablated mice (Figures 7N and 7O).

Figure 6. Single-Cell Analysis Identifies Intratumoral Cell Populations and Confirms Connection of CDK7 Inhibition in Tumor-Intrinsic Signaling to Immunity

- (A) UMAP plot showing identified cell populations within whole tumor from all groups merged.
- (B) Cluster dendrogram showing the lineage hierarchy of identified cell populations in (A).
- (C) UMAP plots of cancer and infiltrating cells displaying marker gene expression.
- (D) UMAP plot showing the cell distribution within identified cell populations upon treatment.
- (E) Distribution fraction of cancer, immune, and stromal compartments in response to indicated treatment.
- (F) Inferred dynamic phases of cell-cycle progression from scRNA-seq analysis.
- (G) Bar plot showing cellular distribution within the cell-cycle progression states indicated in (F).
- (H and I) GSEA of the differentially expressed genes induced by YKL-5-124 *in vivo*. Shown are two of the top most negatively (H) and positively (I) regulated “hallmark” signatures.
- (J) Heatmap for most differentially expressed genes from the top positively regulated pathways (colors are log₂FC).

See also Figure S7.

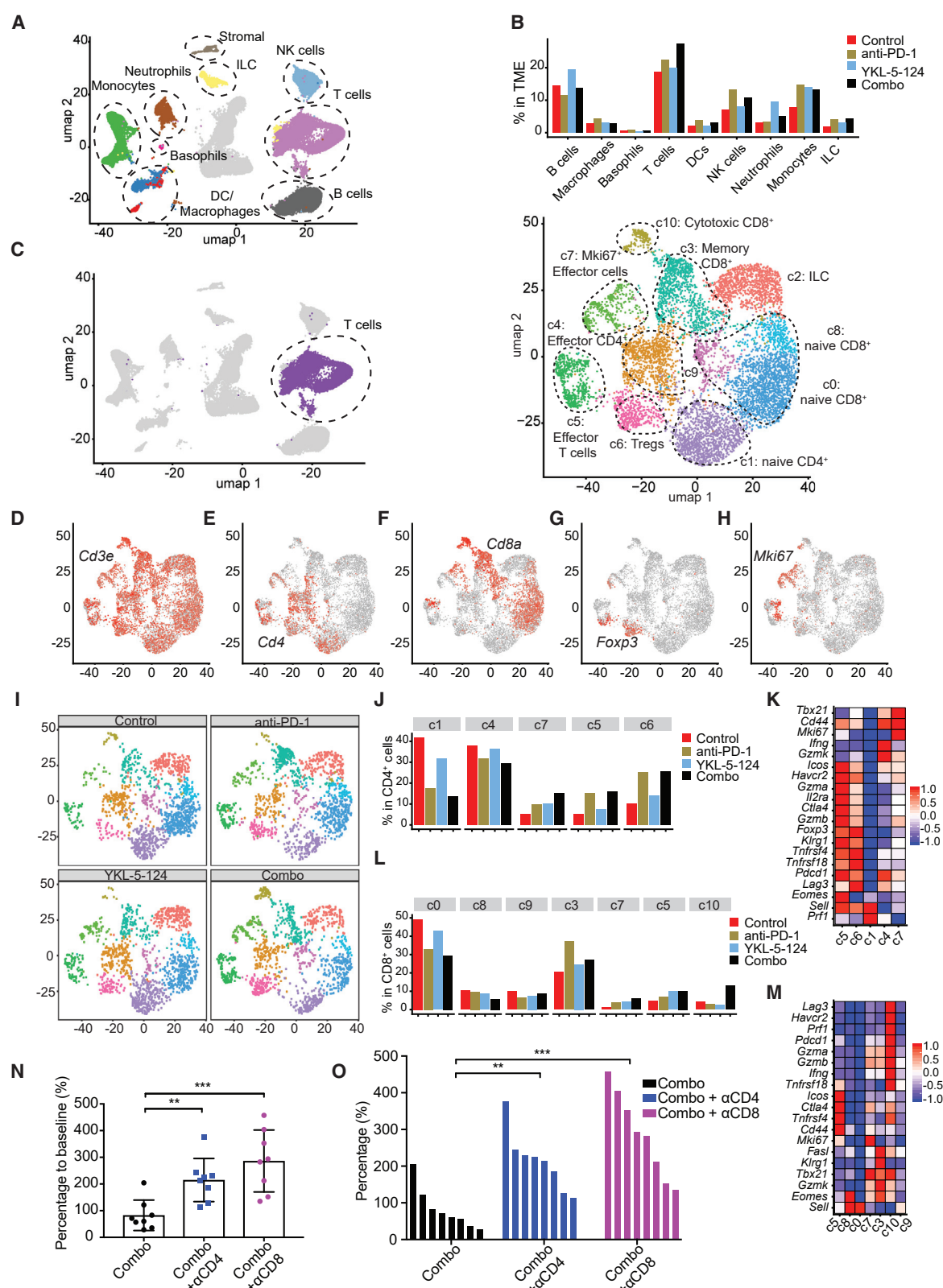


Figure 7. Combinatorial Therapy Reinvigorates Anti-tumor Immunity

(A) UMAP plot of the identified intratumoral infiltrating immune cells.

(B) Percentage of different intratumoral infiltrating immune populations identified in (A).

(legend continued on next page)

Depleting either CD4⁺ or CD8⁺ T cells mitigated the anti-tumor effect of combining YKL-5-124 and anti-PD-1 (Figures 7N and 7O). These observations further support our findings that T cells are required for anti-tumor immunity induced by combination treatment.

DISCUSSION

The FDA recently approved atezolizumab (anti-PD-L1) in combination with chemotherapy for the first-line treatment of patients with ES-SCLC (Horn et al., 2018). Unfortunately, the added benefit to median OS was only ~2 months, highlighting the need for new drug combinations that can potentiate ICBs in SCLC. Recent work in preclinical models suggests that targeting DNA-damage response could potentially enhance ICB in SCLC (Sen et al., 2019).

In this study, we demonstrate that targeting CDK7 with the new selective inhibitor YKL-5-124 disrupts cell-cycle progression and causes DNA replicative stress and genome instability in tumor cells, leading to cellular responses including release of multiple pro-inflammatory cytokines/chemokines. These tumor cell-intrinsic events provoke a robust immune surveillance, which leads to T cell-mediated tumor control in mouse SCLC models. Combining YKL-5-124 with PD-1 blockade promotes strong anti-tumor immunity and confers remarkable survival benefit in this highly aggressive cancer. Our findings provide a rationale for combining CDK7 inhibition and immunotherapy for SCLC patients.

In line with recent work (Olson et al., 2019), selectively targeting CDK7 by YKL-5-124 did not result in changes in CTD phosphorylation of RNA Pol II and SE-associated gene expression in SCLC. These findings reveal potential redundancies in CDK control of gene transcription. YKL-5-124 treatment leads to cells predominantly arrested at the G₁-to-S phase transition and unable to advance to S phase. Conventionally, at the G₁/S transition CDKs activate and facilitate the conversion of MCMs in the pre-initiation complex to an active DNA helicase, leading to initiation of DNA synthesis (Hills and Diffley, 2014; Hyrien, 2016). When the regulatory mechanisms fail, replicative stress and DNA damage ensue (Hills and Diffley, 2014). CDK7 inhibition dramatically impairs the levels of MCM2 at the replication forks, leading to decreased replication origins, elevated replicative stress, and DNA damage. Genome instability such as micronuclei formation has recently emerged as a crucial cue to activate immune response (Harding et al., 2017; Mackenzie et al., 2017). These micronuclei represent an important source of immunostimulatory

DNA and precede activation of inflammatory signaling. Indeed, the series of events provoked by CDK7 inhibition in cancer cells trigger robust immune-response signaling and secretion of pro-inflammatory factors, which potentiates T cell activity, resulting in tumor control.

Importantly, we explored the therapeutic potential of combining CDK7 inhibitor with ICB in murine models with lung TME to closely mimic human disease. A key strength of this current study lies in the use of four histopathology-validated SCLC models. Of note, combining YKL-5-124 with anti-PD-1 significantly improved efficacy and extended OS in all tested SCLC models, supporting the potential of CDK7 inhibition in enhancing immunity as a backbone for combinational immunotherapy. Strikingly, adding YKL-5-125 and anti-PD-1 to standard chemotherapy resulted in the best tumor response and the longest survival among all treatment groups, with no observed toxicities. This data provides strong evidence for combining CDK7 inhibitor in first-line treatment with chemotherapy and ICB in clinical trials and highlights the translational significance of our study.

Our current understanding of the TME in SCLC is poor. To the best of our knowledge, this is the first unbiased scRNA-seq analysis of TME in mouse SCLC, which was performed without prior marker selection. In the cancer cells, scRNA-seq analysis confirms a unique signature of disrupted cell-cycle progression and connects the tumor-intrinsic effect by YKL-5-124 to immune-response signaling. Our study uncovered several key observations and mechanisms of action on immune compartments: (1) complexity of tumor immune ecosystem dynamics; YKL-5-124, anti-PD-1, and combination therapy (2) trigger the expansion/reduction of certain subtypes of tumor-infiltrating lymphoid and myeloid cells, (3) cause a dramatic shift of naive CD4⁺ and CD8⁺ T cells to effector/activated T cells, and (4) enhance proliferative capacity of Mki67⁺ effector T cells; combination therapy (5) results in the most prominent increase of CD8⁺ CTLs and (6) triggers the strongest increase in the expression of an anti-tumor cytotoxic gene signature. Further work is needed to fully elucidate CDK7 function in immune cells.

In summary, our work serves as the basis for the combinatorial application of CDK7 inhibitor and immunotherapy and provides evidence for combining YKL-5-124 and PD-1 blockade in future SCLC clinical trials. Considering the universal role of CDK7 in genome instability, combining CDK7 inhibition with ICB might improve anti-tumor immunity as a widely applicable new approach in cancer immunotherapy.

(C) UMAP plot highlighting the whole population of T cells identified in (A) in purple (left) and UMAP plot showing the subpopulations identified within the T cells (right).

(D–H) UMAP plots of T cells displaying select marker gene expression.

(I) UMAP density plots showing distribution of annotated clusters in (C) within intratumoral T cells upon treatment.

(J) Percentage of cells in individual CD4⁺ T clusters annotated in (C) by treatment.

(K) Heatmap displaying expression of select genes in CD4⁺ T cell clusters (colors are log₂FC).

(L) Percentage of cells in individual CD8⁺ T cell clusters annotated in (C) by treatment.

(M) Heatmap displaying expression of select genes in CD8⁺ T cell clusters (colors are log₂FC).

(N) Percentages of tumor volume after 2 weeks of treatment combining anti-PD-1 and YKL-5-124 (Combo) with or without α CD4 (400 μ g/mouse) or α CD8 (400 μ g/mouse) antibodies ($n = 8$). Data shown as means \pm SD. ** $p < 0.01$, *** $p < 0.001$ (unpaired two-tailed t test).

(O) Waterfall plot shows tumor response after week 2. Each column represents one mouse, in comparison with baseline measurements ($n = 8$). ** $p < 0.01$, *** $p < 0.001$ (unpaired two-tailed t test).

See also Figure S7.

STAR★METHODS

Detailed methods are provided in the online version of this paper and include the following:

- **KEY RESOURCES TABLE**
- **LEAD CONTACT AND MATERIALS AVAILABILITY**
- **EXPERIMENTAL MODEL AND SUBJECT DETAILS**
 - Animal Studies
 - Cell Lines
- **METHOD DETAILS**
 - Chemicals
 - *In Vivo* Toxicity Evaluation and Treatment Studies
 - Cell Viability Assay
 - Cell Cycle Analysis
 - BrdU Analysis
 - RNA Extraction and RT-qPCR
 - Protein Extraction and Western Blotting Analysis
 - Competitive Pull-down Assay for YKL-5-124 Target Engagement
 - Immunofluorescence Staining and Imaging
 - EdU and MCM2 Imaging by the Stochastic Reconstruction Microscopy (STORM)
 - Histology and Immunohistochemistry
 - Luminex Analysis of Murine BAL Fluid
 - MRI Quantification
 - Immune Profiling Flow Cytometry
 - *Ex Vivo* OT-I T Cell Assay
 - Generation of cGAS CRISPR/Cas9 Knockout
 - Bulk-RNA Sequencing Analysis
 - Single-Cell RNA Sequencing
 - Illustration Tool
- **QUANTIFICATION AND STATISTICAL ANALYSIS**
- **DATA AND CODE AVAILABILITY**

SUPPLEMENTAL INFORMATION

Supplemental Information can be found online at <https://doi.org/10.1016/j.ccr.2019.11.003>.

ACKNOWLEDGMENTS

We thank the NYU Langone Health Preclinical Imaging Laboratory (partially funded by National Institutes of Health (NIH)/National Cancer Institute (NCI) 5P30CA016087 and NIH P41 EB017183) and the Genome Technology Center (partially supported by P30CA016087) for library preparation and sequencing. This work is supported by a Lung Cancer Research Foundation grant (H.Z.), NCI/NIH K99CA201618 (C.L.C.), K08CA222657 (M.G.O.), U01CA213333 (K.K.W. and N.S.G.), and P01 CA154303 (K.K.W.). This work is also supported by the Bridge Project (K.K.W. and N.S.G.), a collaboration between The Koch Institute for Integrative Cancer Research at MIT and the Dana-Farber/Harvard Cancer Center (DF/HCC).

AUTHOR CONTRIBUTIONS

H.Z., C.L.C., R.D., N.S.G., and K.K.W. supervised the work, designed all the experiments, and interpreted the data. H.Z., C.L.C., R.D., M.G.O., J.D., B.D., F.L., Y.P., K.J., A.R.R., T.C., M.B., and C.M.D. conducted experiments. E.P., V.P., C.T., and H.S. performed MRI. R.D., D.M.C., G.-C.Y., and R.B. performed bioinformatics analysis. N.K., T.Z., and Z.H. contributed to compound synthesis. X.Z., Y.Y., and E.R. conducted single-cell imaging. H.Z. and K.E.L. conducted MRI analysis. M.G.O., V.O.S., G.M., K.D.S., A.K., A.J.A., and W.G.K. provided critical expertise and/or reagents. All the au-

thors contributed to manuscript preparation. H.Z., C.L.C., R.D., and K.K.W. wrote the manuscript.

DECLARATION OF INTERESTS

K.K.W. is a founder and equity holder of G1 Therapeutics and has sponsored research agreements with MedImmune, Takeda, TargImmune, Bristol-Myers Squibb (BMS), Mirati, Merus, and Alkermes, and consulting and sponsored research agreements with AstraZeneca, Janssen, Pfizer, Novartis, Merck, Ono, and Array. N.G.S. is a founder, science advisory board member and equity holder in Gatekeeper, Syros, Petra, C4, B2S, and Soltego. The Gray lab receives or has received research funding from Novartis, Takeda, Astellas, Taiho, Janssen, Kinogen, Voronoi, Her2IIC, Deerfield, and Sanofi. G.M. has research contract agreements with GlaxoSmithKline, Pfizer, and Puretech Health. V.V. has an advisory/consulting role at Genentech, Merck, BMS, AstraZeneca, Foundation Medicine, Nektar Therapeutics, Alkermes, Reddy labs, and Millennium pharma. M.G.O. is a consultant for HVH precision analytics, and has research funding from AstraZeneca and Eli Lilly and Company. H.Z., C.L.C., N.S.G., and K.K.W. have ownership interest in a patent application.

Received: April 12, 2019

Revised: September 23, 2019

Accepted: November 22, 2019

Published: December 26, 2019

REFERENCES

- Alexandrov, L.B., Nik-Zainal, S., Wedge, D.C., Aparicio, S.A., Behjati, S., Biankin, A.V., Bignell, G.R., Bolli, N., Borg, A., Borresen-Dale, A.L., et al. (2013). Signatures of mutational processes in human cancer. *Nature* **500**, 415–421.
- Aran, D., Looney, A.P., Liu, L., Wu, E., Fong, V., Hsu, A., Chak, S., Naikawadi, R.P., Wolters, P.J., Abate, A.R., et al. (2019). Reference-based analysis of lung single-cell sequencing reveals a transitional profibrotic macrophage. *Nat. Immunol.* **20**, 163–172.
- Asghar, U., Witkiewicz, A.K., Turner, N.C., and Knudsen, E.S. (2015). The history and future of targeting cyclin-dependent kinases in cancer therapy. *Nat. Rev. Drug Discov.* **14**, 130–146.
- Bakhour, S.F., and Cantley, L.C. (2018). The multifaceted role of chromosomal instability in cancer and its microenvironment. *Cell* **174**, 1347–1360.
- Barilla, R.M., Diskin, B., Caso, R.C., Lee, K.B., Mohan, N., Buttar, C., Adam, S., Sekendiz, Z., Wang, J., Salas, R.D., et al. (2019). Specialized dendritic cells induce tumor-promoting IL-10(+)IL-17(+) FoxP3(neg) regulatory CD4(+) T cells in pancreatic carcinoma. *Nat. Commun.* **10**, 1424.
- Becht, E., McInnes, L., Healy, J., Dutertre, C.A., Kwok, I.W.H., Ng, L.G., Ginhoux, F., and Newell, E.W. (2018). Dimensionality reduction for visualizing single-cell data using UMAP. *Nat. Biotechnol.* **37**, 38–44.
- Borst, J., Ahrends, T., Babala, N., Melief, C.J.M., and Kastenmuller, W. (2018). CD4(+) T cell help in cancer immunology and immunotherapy. *Nat. Rev. Immunol.* **18**, 635–647.
- Brunner, C., Seiderer, J., Schlamp, A., Bidlingmaier, M., Eigler, A., Haimerl, W., Lehr, H.A., Krieg, A.M., Hartmann, G., and Endres, S. (2000). Enhanced dendritic cell maturation by TNF-alpha or cytidine-phosphate-guanosine DNA drives T cell activation in vitro and therapeutic anti-tumor immune responses in vivo. *J. Immunol.* **165**, 6278–6286.
- Bunn, P.A., Jr., Minna, J.D., Augustyn, A., Gazdar, A.F., Ouadah, Y., Krasnow, M.A., Berns, A., Brambilla, E., Rekhtman, N., Massion, P.P., et al. (2016). Small cell lung cancer: can recent advances in biology and molecular biology be translated into improved outcomes? *J. Thorac. Oncol.* **11**, 453–474.
- Butler, A., Hoffman, P., Smibert, P., Papalexis, E., and Satija, R. (2018). Integrating single-cell transcriptomic data across different conditions, technologies, and species. *Nat. Biotechnol.* **36**, 411–420.
- Carney, D.N., Bunn, P.A., Jr., Gazdar, A.F., Pagan, J.A., and Minna, J.D. (1981). Selective growth in serum-free hormone-supplemented medium of tumor cells obtained by biopsy from patients with small cell carcinoma of the lung. *Proc. Natl. Acad. Sci. U S A* **78**, 3185–3189.

- Christensen, C.L., Kwiatkowski, N., Abraham, B.J., Carretero, J., Al-Shahrour, F., Zhang, T., Chipumuro, E., Herter-Sprie, G.S., Akbay, E.A., Altabef, A., et al. (2014). Targeting transcriptional addictions in small cell lung cancer with a covalent CDK7 inhibitor. *Cancer Cell* 26, 909–922.
- Dobin, A., Davis, C.A., Schlesinger, F., Drenkow, J., Zaleski, C., Jha, S., Batut, P., Chaisson, M., and Gingeras, T.R. (2013). STAR: ultrafast universal RNA-seq aligner. *Bioinformatics* 29, 15–21.
- Ebert, P.J.R., Cheung, J., Yang, Y., McNamara, E., Hong, R., Moskalenko, M., Gould, S.E., Maecker, H., Irving, B.A., Kim, J.M., et al. (2016). MAP kinase inhibition promotes T cell and anti-tumor activity in combination with PD-L1 checkpoint blockade. *Immunity* 44, 609–621.
- Fisher, R.P., and Morgan, D.O. (1994). A novel cyclin associates with MO15/CDK7 to form the CDK-activating kinase. *Cell* 78, 713–724.
- Ganuza, M., Saiz-Ladera, C., Canamero, M., Gomez, G., Schneider, R., Blasco, M.A., Pisano, D., Paramio, J.M., Santamaría, D., and Barbacid, M. (2012). Genetic inactivation of Cdk7 leads to cell cycle arrest and induces premature aging due to adult stem cell exhaustion. *EMBO J.* 31, 2498–2510.
- George, J., Lim, J.S., Jang, S.J., Cun, Y., Ozretic, L., Kong, G., Leenders, F., Lu, X., Fernandez-Cuesta, L., Bosco, G., et al. (2015). Comprehensive genomic profiles of small cell lung cancer. *Nature* 524, 47–53.
- Glover-Cutter, K., Larochelle, S., Erickson, B., Zhang, C., Shokat, K., Fisher, R.P., and Bentley, D.L. (2009). TFIIB-associated Cdk7 kinase functions in phosphorylation of C-terminal domain Ser7 residues, promoter-proximal pausing, and termination by RNA polymerase II. *Mol. Cell. Biol.* 29, 5455–5464.
- Gubin, M.M., Esaulova, E., Ward, J.P., Malkova, O.N., Runci, D., Wong, P., Noguchi, T., Arthur, C.D., Meng, W., Alspach, E., et al. (2018). High-dimensional analysis delineates myeloid and lymphoid compartment remodeling during successful immune-checkpoint cancer therapy. *Cell* 175, 1014–1030.e19.
- Harding, S.M., Benci, J.L., Irianto, J., Discher, D.E., Minn, A.J., and Greenberg, R.A. (2017). Mitotic progression following DNA damage enables pattern recognition within micronuclei. *Nature* 548, 466–470.
- Harper, J.W., and Elledge, S.J. (1998). The role of Cdk7 in CAK function, a retro-perspective. *Genes Dev.* 12, 285–289.
- Hellmann, M.D., Callahan, M.K., Awad, M.M., Calvo, E., Ascierto, P.A., Atmaca, A., Rizvi, N.A., Hirsch, F.R., Selvaggi, G., Szustakowski, J.D., et al. (2018). Tumor mutational burden and efficacy of Nivolumab monotherapy and in combination with Ipilimumab in small-cell lung cancer. *Cancer Cell* 33, 853–861.e4.
- Herndler-Brandstetter, D., Ishigame, H., Shinnakasu, R., Plajer, V., Stecher, C., Zhao, J., Lietzenmayer, M., Kroehling, L., Takumi, A., Kometani, K., et al. (2018). KLRLG1(+) effector CD8(+) T cells lose KLRLG1, differentiate into all memory T cell lineages, and convey enhanced protective immunity. *Immunity* 48, 716–729.e8.
- Hills, S.A., and Diffley, J.F. (2014). DNA replication and oncogene-induced replicative stress. *Curr. Biol.* 24, R435–R444.
- Hogquist, K.A., Jameson, S.C., Heath, W.R., Howard, J.L., Bevan, M.J., and Carbone, F.R. (1994). T cell receptor antagonist peptides induce positive selection. *Cell* 76, 17–27.
- Horn, L., Mansfield, A.S., Szczesna, A., Havel, L., Krzakowski, M., Hochmair, M.J., Huemer, F., Losonczy, G., Johnson, M.L., Nishio, M., et al. (2018). First-line atezolizumab plus chemotherapy in extensive-stage small-cell lung cancer. *N. Engl. J. Med.* 379, 2220–2229.
- Huang, F., Hartwich, T.M., Rivera-Molina, F.E., Lin, Y., Duim, W.C., Long, J.J., Uchil, P.D., Myers, J.R., Baird, M.A., Mothes, W., et al. (2013). Video-rate nanoscopy using sCMOS camera-specific single-molecule localization algorithms. *Nat. Methods* 10, 653–658.
- Hyrien, O. (2016). How MCM loading and spreading specify eukaryotic DNA replication initiation sites. *F1000Res.* 5, <https://doi.org/10.12688/f1000research.9008.1>.
- Kanin, E.I., Kipp, R.T., Kung, C., Slattery, M., Viale, A., Hahn, S., Shokat, K.M., and Ansari, A.Z. (2007). Chemical inhibition of the TFIIB-associated kinase Cdk7/Kin28 does not impair global mRNA synthesis. *Proc. Natl. Acad. Sci. U S A* 104, 5812–5817.
- Kwiatkowski, N., Zhang, T., Rahl, P.B., Abraham, B.J., Reddy, J., Ficarro, S.B., Dastur, A., Amzallag, A., Ramaswamy, S., Tesar, B., et al. (2014). Targeting transcription regulation in cancer with a covalent CDK7 inhibitor. *Nature* 511, 616–620.
- Larochelle, S., Amat, R., Glover-Cutter, K., Sanso, M., Zhang, C., Allen, J.J., Shokat, K.M., Bentley, D.L., and Fisher, R.P. (2012). Cyclin-dependent kinase control of the initiation-to-elongation switch of RNA polymerase II. *Nat. Struct. Mol. Biol.* 19, 1108–1115.
- Larochelle, S., Merrick, K.A., Terret, M.E., Wohlbond, L., Barboza, N.M., Zhang, C., Shokat, K.M., Jallepalli, P.V., and Fisher, R.P. (2007). Requirements for Cdk7 in the assembly of Cdk1/cyclin B and activation of Cdk2 revealed by chemical genetics in human cells. *Mol. Cell* 25, 839–850.
- Liao, Y., Smyth, G.K., and Shi, W. (2014). featureCounts: an efficient general purpose program for assigning sequence reads to genomic features. *Bioinformatics* 30, 923–930.
- Love, M.I., Huber, W., and Anders, S. (2014). Moderated estimation of fold change and dispersion for RNA-seq data with DESeq2. *Genome Biol.* 15, 550.
- Lun, A.T., McCarthy, D.J., and Marioni, J.C. (2016). A step-by-step workflow for low-level analysis of single-cell RNA-seq data with Bioconductor. *F1000Res.* 5, 2122.
- Mackenzie, K.J., Carroll, P., Martin, C.A., Murina, O., Fluteau, A., Simpson, D.J., Olova, N., Sutcliffe, H., Rainger, J.K., Leitch, A., et al. (2017). cGAS surveillance of micronuclei links genome instability to innate immunity. *Nature* 548, 461–465.
- McCarthy, D.J., Campbell, K.R., Lun, A.T., and Wills, Q.F. (2017). Scater: pre-processing, quality control, normalization and visualization of single-cell RNA-seq data in R. *Bioinformatics* 33, 1179–1186.
- Merrick, K.A., Larochelle, S., Zhang, C., Allen, J.J., Shokat, K.M., and Fisher, R.P. (2008). Distinct activation pathways confer cyclin-binding specificity on Cdk1 and Cdk2 in human cells. *Mol. Cell* 32, 662–672.
- Olson, C.M., Liang, Y., Leggett, A., Park, W.D., Li, L., Mills, C.E., Elsarrag, S.Z., Ficarro, S.B., Zhang, T., Duster, R., et al. (2019). Development of a selective CDK7 covalent inhibitor reveals predominant cell-cycle phenotype. *Cell Chem. Biol.* 26, 792–803.e10.
- Oser, M.G., Sabet, A.H., Gao, W., Chakraborty, A.A., Schinzel, A.C., Jennings, R.B., Fonseca, R., Bonal, D.M., Booker, M.A., Flaihel, A., et al. (2019). The KDM5A/RBP2 histone demethylase represses NOTCH signaling to sustain neuroendocrine differentiation and promote small cell lung cancer tumorigenesis. *Genes Dev.* <https://doi.org/10.1101/gad.328336.119>.
- Ritchie, M.E., Phipson, B., Wu, D., Hu, Y., Law, C.W., Shi, W., and Smyth, G.K. (2015). Limma powers differential expression analyses for RNA-sequencing and microarray studies. *Nucleic Acids Res.* 43, e47.
- Rust, M.J., Bates, M., and Zhuang, X. (2006). Sub-diffraction-limit imaging by stochastic optical reconstruction microscopy (STORM). *Nat. Methods* 3, 793–795.
- Salmon, H., Idoyaga, J., Rahman, A., Leboeuf, M., Remark, R., Jordan, S., Casanova-Acebes, M., Khudoyazarova, M., Agudo, J., Tung, N., et al. (2016). Expansion and activation of CD103(+) dendritic cell progenitors at the tumor site enhances tumor responses to therapeutic PD-L1 and BRAF inhibition. *Immunity* 44, 924–938.
- Schachter, M.M., and Fisher, R.P. (2013). The CDK-activating kinase Cdk7: taking yes for an answer. *Cell Cycle* 12, 3239–3240.
- Schachter, M.M., Merrick, K.A., Larochelle, S., Hirsch, A., Zhang, C., Shokat, K.M., Rubin, S.M., and Fisher, R.P. (2013). A Cdk7-Cdk4 T-loop phosphorylation cascade promotes G1 progression. *Mol. Cell* 50, 250–260.
- Schaffer, B.E., Park, K.S., Yiu, G., Conklin, J.F., Lin, C., Burkhardt, D.L., Karnezis, A.N., Sweet-Cordero, E.A., and Sage, J. (2010). Loss of p130 accelerates tumor development in a mouse model for human small-cell lung carcinoma. *Cancer Res.* 70, 3877–3883.
- Schreiber, R.D., Old, L.J., and Smyth, M.J. (2011). Cancer immunoediting: integrating immunity's roles in cancer suppression and promotion. *Science* 331, 1565–1570.

- Scialdone, A., Natarajan, K.N., Saraiva, L.R., Proserpio, V., Teichmann, S.A., Stegle, O., Marioni, J.C., and Buettner, F. (2015). Computational assignment of cell-cycle stage from single-cell transcriptome data. *Methods* 85, 54–61.
- Semenova, E.A., Nagel, R., and Berns, A. (2015). Origins, genetic landscape, and emerging therapies of small cell lung cancer. *Genes Dev.* 29, 1447–1462.
- Sen, T., Rodriguez, B.L., Chen, L., Corte, C.M.D., Morikawa, N., Fujimoto, J., Cristea, S., Nguyen, T., Diao, L., Li, L., et al. (2019). Targeting DNA damage response promotes antitumor immunity through STING-mediated T-cell activation in small cell lung cancer. *Cancer Discov.* 9, 646–661.
- Sengupta, P., Jovanovic-Talisman, T., Skoko, D., Renz, M., Veatch, S.L., and Lippincott-Schwartz, J. (2011). Probing protein heterogeneity in the plasma membrane using PALM and pair correlation analysis. *Nat. Methods* 8, 969–975.
- Serizawa, H., Conaway, J.W., and Conaway, R.C. (1993). Phosphorylation of C-terminal domain of RNA polymerase II is not required in basal transcription. *Nature* 363, 371–374.
- Serizawa, H., Makela, T.P., Conaway, J.W., Conaway, R.C., Weinberg, R.A., and Young, R.A. (1995). Association of Cdk-activating kinase subunits with transcription factor TFIIH. *Nature* 374, 280–282.
- Sharma, P., and Allison, J.P. (2015). The future of immune checkpoint therapy. *Science* 348, 56–61.
- Shiekhattar, R., Mermelstein, F., Fisher, R.P., Drapkin, R., Dynlacht, B., Wessling, H.C., Morgan, D.O., and Reinberg, D. (1995). Cdk-activating kinase complex is a component of human transcription factor TFIIH. *Nature* 374, 283–287.
- Spranger, S., Dai, D., Horton, B., and Gajewski, T.F. (2017). Tumor-residing Batf3 dendritic cells are required for effector T cell trafficking and adoptive T cell therapy. *Cancer Cell* 31, 711–723.e4.
- Subramanian, A., Tamayo, P., Mootha, V.K., Mukherjee, S., Ebert, B.L., Gillette, M.A., Paulovich, A., Pomeroy, S.L., Golub, T.R., Lander, E.S., and Mesirov, J.P. (2005). Gene set enrichment analysis: a knowledge-based approach for interpreting genome-wide expression profiles. *Proc. Natl. Acad. Sci. U S A* 102, 15545–15550.
- van Meerbeeck, J.P., Fennell, D.A., and De Ruysscher, D.K. (2011). Small-cell lung cancer. *Lancet* 378, 1741–1755.
- Veatch, S.L., Machta, B.B., Shelby, S.A., Chiang, E.N., Holowka, D.A., and Baird, B.A. (2012). Correlation functions quantify super-resolution images and estimate apparent clustering due to over-counting. *PLoS One* 7, e31457.
- Yin, Y., Lee, W.T.C., and Rothenberg, E. (2019). Ultrafast data mining of molecular assemblies in multiplexed high-density super-resolution images. *Nat. Commun.* 10, 119.
- Yoshihara, K., Shahmoradgoli, M., Martinez, E., Vegesna, R., Kim, H., Torres-Garcia, W., Trevino, V., Shen, H., Laird, P.W., Levine, D.A., et al. (2013). Inferring tumour purity and stromal and immune cell admixture from expression data. *Nat. Commun.* 4, 2612.
- Zhang, T., Kwiatkowski, N., Olson, C.M., Dixon-Clarke, S.E., Abraham, B.J., Greifenberg, A.K., Ficarro, S.B., Elkins, J.M., Liang, Y., Hannett, N.M., et al. (2016). Covalent targeting of remote cysteine residues to develop CDK12 and CDK13 inhibitors. *Nat. Chem. Biol.* 12, 876–884.
- Zheng, G.X., Terry, J.M., Belgrader, P., Ryvkin, P., Bent, Z.W., Wilson, R., Ziraldo, S.B., Wheeler, T.D., McDermott, G.P., Zhu, J., et al. (2017). Massively parallel digital transcriptional profiling of single cells. *Nat. Commun.* 8, 14049.

STAR★METHODS

KEY RESOURCES TABLE

REAGENT or RESOURCE	SOURCE	IDENTIFIER
Antibodies		
Goat IRDye 680RD anti-Mouse IgG	LI-COR Biosciences	Cat#926-68070; RRID: AB_10956589
Goat IRDye 800CW anti-Rabbit IgG	LI-COR Biosciences	Cat#926-32211; RRID: AB_10796098
CDK7	Cell Signaling Technology	Cat#2916; RRID: AB_2077142
Cyclin H	Bethyl Labs	Cat#A301-674A; RRID: AB_1210922
Cyclin K	Bethyl Labs	Cat#A301-939A; RRID: AB_1547934
pCDK2 T160	Cell Signaling Technology	Cat#2561; RRID: AB_2078685
pCDK1 T161	Cell Signaling Technology	Cat#9114; RRID: AB_2074652
CDK1	Cell Signaling Technology	Cat#77055; RRID: AB_2716331
CDK2	Cell Signaling Technology	Cat#2546; RRID: AB_2276129
CDK1/2	Santa Cruz	Cat#sc-53219; RRID: AB_2120095
Tubulin	Cell Signaling Technology	Cat#3873; RRID: AB_1904178
pCTD Ser2	Millipore	Cat#04-1571; RRID: AB_11212363
pCTD Ser5	Millipore	Cat#04-1572; RRID: AB_10615822
Total RNA Polymerase II	Bethyl Labs	Cat#3A300-653A; RRID: AB_2779369
Cyclin E D7T3U	Cell Signaling Technology	Cat#20808; RRID: AB_2783554
Cyclin E HE12	Cell Signaling Technology	Cat#4129; RRID: AB_2071200
Anti-MCM2 antibody [EPR4120]	Abcam	Cat#ab223403
Anti-PCNA	Santa Cruz	Cat#sc-56; RRID: AB_628110
γH2AX	Cell Signaling Technology	Cat#9718S; RRID: AB_2118009
ASCL1	Abcam	Cat#ab211327
MYC	Abcam	Cat#ab32072; RRID: AB_731658
STING (22P2F)	Cell Signaling Technology	Cat#13647S; RRID: AB_2732796
pSTING (S365) (D8F4W)	Cell Signaling Technology	Cat#72971S; RRID: AB_2799831
IRF3 (D83B9)	Cell Signaling Technology	Cat#4302S; RRID: AB_1904036
pIRF3 (S396) (4D4G)	Cell Signaling Technology	Cat#4947S; RRID: AB_823547
pTBK1 (S172) (D52C2)	Cell Signaling Technology	Cat#5483S; RRID: AB_10693472
Actin Clone AC-15	Sigma-Aldrich	Cat#A5441; RRID: AB_476744
STING	Cell Signaling Technology	Cat#13647; RRID: AB_2732796
Phospho-STING	Cell Signaling Technology	Cat#50907
IRF3	Cell Signaling Technology	Cat#4302; RRID: AB_1904036
pIRF3	Cell Signaling Technology	Cat#37829; RRID: AB_2799121
TBK1	Cell Signaling Technology	Cat#3504; RRID: AB_2255663
IKKε	Cell Signaling Technology	Cat#2905; RRID: AB_1147662
pIKKε	Cell Signaling Technology	Cat#8766; RRID: AB_2737061
InVivoMAb anti-mouse CD8α (clone 2.43)	Bio X Cell	BE0061; RRID: AB_1125541
InVivoMAb anti-mouse CD4 (clone GK1.5)	Bio X Cell	BE0003-1; RRID: AB_1107636
InVivoMAb rat IgG2b isotype control	Bio X Cell	BE0090; RRID: AB_1107780
anti-mouse PD-1 (CD279) (Clone: 29F.1A12)	Gordon J. Freeman, DFCI	N/A
CD45 (clone 30-F11)	BioLegend	103155; RRID: AB_2650656
CD3 (clone 17A2)	BioLegend	100216; RRID: AB_493697
CD4 (clone GK1.5)	BioLegend	100453; RRID: AB_2565843
CD8 (clone 53-6.7)	BioLegend	100759; RRID: AB_2563510
CD11b (clone M1/70)	BioLegend	101242; RRID: AB_2563310

(Continued on next page)

Continued

REAGENT or RESOURCE	SOURCE	IDENTIFIER
CD11c (clone N418)	BioLegend	117336; RRID: AB_2565268
CD103 (clone 2E7)	BioLegend	121425; RRID: AB_2563690
Ki67 (clone 16A8)	BioLegend	652411; RRID: AB_2562663
CD44 (clone IM7)	BioLegend	103032; RRID: AB_2076204
CD62L (clone MEL-14)	BioLegend	104417; RRID: AB_313102
TNF α (MP6-XT22)	BioLegend	506304; RRID: AB_315425
IFN γ (XMG1.2)	BioLegend	505826; RRID: AB_2295770
Chemicals, Peptides, and Recombinant Proteins		
YKL-5-124	Olson et al., 2019	N/A
THZ531	Zhang et al., 2016	N/A
THZ1	Kwiatkowski et al., 2014	N/A
Cisplatin	TEVA PHARMACEUTICALS	Cat#18E01LA
Etoposide	Accord Healthcare, Inc.	Cat#X15146
Biotinylated-THZ1 (Bio-THZ)	Kwiatkowski et al., 2014	N/A
CCK8 reagent	Dojindo	Cat#CK04
Odyssey Blocking Buffer	LI-COR	Cat#927-50003
Propidium Iodide	Sigma-Aldrich	Cat#P4864
Halt™ Protease and Phosphatase Inhibitor Cocktail	Thermo Fisher Scientific	Cat#78440
TaqMan Gene Expression Master Mix	Life Technologies	Cat#4369514
RIPA lysis buffer	Thermo Fisher Scientific	Cat#89900
IDIM media	Thermo Fisher Scientific	Cat#12440061
RPMI media	Thermo Fisher Scientific	Cat#11875093
Ovalbumin peptide residues 257-264	GenScript	Cat#RP10611
Collagenase D	Sigma-Aldrich	Cat#11088866001
Dnase 1	Sigma-Aldrich	Cat#10104159001
RBC Lysis Buffer	BioLegend	Cat#420301
BD Cytofix/Cytoperm	BD Biosciences	Cat#554722
SYBR Green Master Mix	Thermo Fisher Scientific	Cat#A25742
Lipofectamine 3000	Thermo Fisher Scientific	Cat#L3000015
Glucose Oxidase	Sigma-Aldrich	Cat#2133
Catalase	Sigma-Aldrich	Cat#C3155
Glucose	Sigma-Aldrich	Cat#G8270
Cysteamine	Fisher Scientific	BP2664100
Citrate Buffer (Dako Target Retrieval Solution)	Dako	Cat#S1699
Leica Novolink Polymer	Leica	Cat#RE7161
Critical Commercial Assays		
Rneasy Plus Mini Kit	QIAGEN	Cat#74136
BrdU assay	BD Biosciences	Cat#559619
High-Capacity RNA-to-cDNA™ Kit	Thermo Fisher Scientific	Cat#4387406
UltraComp eBeads™ Compensation Beads	Thermo Fisher Scientific	01-2222-42
ArC™ Amine Reactive Compensation Bead Kit	Thermo Fisher Scientific	A10628
Cytokine/Chemokine 32-plex Assay	Millipore	MCYTMMAG-70K-PX32
Pierce™ BCA Protein Assay Kit	Thermo Fisher Scientific	Cat#23225
Chromium™ Single Cell 3' Library & Gel Bead Kit v2	10x Genomics	PN-120237
Chromium™ Single Cell Chip Kit	10x Genomics	PN-120236
Chromium™ i7 Multiplex Kit	10x Genomics	PN-120262

(Continued on next page)

Continued

REAGENT or RESOURCE	SOURCE	IDENTIFIER
Deposited Data		
RNA-seq (bulk)	This paper	Accession Number GEO: GSE129299
scRNA-seq	This paper	Accession Number GEO: GSE129299
Experimental Models: Cell Lines		
Human: HAP1	Horizon Discovery	C859
Human: GLC16	Christensen et al., 2014	N/A
Human: NCI-H69	Christensen et al., 2014	N/A
Human: DMS79	Christensen et al., 2014	N/A
Human: NCI-H82	Christensen et al., 2014	N/A
Human: HEK-293T	ATCC	CRL-3216™
Mouse: RPP631	This paper	N/A
Mouse: RPP-MYC	This paper	N/A
Mouse: RP	This paper	N/A
Experimental Models: Organisms/Strains		
C57BL/6J	The Jackson Laboratory	Stock No: 000664
RPP631 Orthotopic Model	This paper	N/A
RPP-MYC Orthotopic Model	This paper	N/A
RP Orthotopic Model	This paper	N/A
RPP GEMM	Schaffer et al., 2010	N/A
OT-I model	The Jackson Laboratory	Stock No: 003831
Oligonucleotides		
See Table S1		
Recombinant DNA		
lentiCRISPR v2	Addgene	Cat#52961
lentiCRISPR v2-sgcGAS	This paper	N/A
psPAX2	Addgene	Cat#12260
pMD2.G	Addgene	Cat#12259
Software and Algorithms		
GraphPad Prism 7	GraphPad Software Inc.	http://www.graphpad.com
ImageStudio Light	ImageStudio Software	https://www.licor.com/bio/image-studio-lite/
R v3.5.1	R Core Team (2016) The R Project for Statistical Computing	http://www.r-project.org
Gene Set Enrichment Analysis (GSEA)	Broad Institute	http://software.broadinstitute.org/gsea/index.jsp
ModFit LT	Verity Software House	https://www.vsh.com/products/mflt/
Fiji NIH	ImageJ	https://imagej.nih.gov/ij/docs/guide/146-2.html
FlowJo	FlowJo Software	https://www.flowjo.com/
STAR (v2.5.2b)	STAR Software	https://github.com/alexdobin/STAR
featureCounts	featureCounts Software	http://bioinf.wehi.edu.au/featureCounts/
Cell Ranger (v1.3)	Cell Ranger Single Cell Software Suite	https://support.10xgenomics.com/single-cell-gene-expression/software/pipelines/latest/what-is-cell-ranger
Seurat (v2.3.4)	Seurat R package	https://satijalab.org/seurat/
Estimate (v1.0.13)	Estimate R package	https://bioinformatics.mdanderson.org/estimate/rpackage.html
SingleR (v0.2.1)	SingleR R package	https://github.com/dviraran/SingleR
uwot (v0.0.0.9010)	Uwot R package	https://github.com/jlmelville/uwot
dbSCAN (v1.1-3)	dbSCAN R package	https://cran.r-project.org/web/packages/dbSCAN/index.html

(Continued on next page)

Continued

REAGENT or RESOURCE	SOURCE	IDENTIFIER
scran (v1.10.1)	scran R package	https://bioconductor.org/packages/release/bioc/html/scran.html
scater (v1.10.0)	scater R package	https://bioconductor.org/packages/release/bioc/html/scater.html
limma (v3.38.2)	limma R package	https://bioconductor.org/packages/release/bioc/html/limma.html
BioRender	BioRender Software	https://biorender.com/

LEAD CONTACT AND MATERIALS AVAILABILITY

Further information and requests for resources and reagents should be directed to and will be fulfilled by the Lead Contact, Kwok-Kin Wong (Kwok_Kin.wong@nyulangone.org).

EXPERIMENTAL MODEL AND SUBJECT DETAILS

Animal Studies

All animal studies were reviewed and approved by the Institutional Animal Care and Use Committee (IACUC) at the New York University Langone Health (NYULH) and Dana-Farber Cancer Institute (DFCI). The GEMM harboring conditional mutant *Rb1*, *p53*, and *p130* (RPP) has been described previously ([Schaffer et al., 2010](#)). From 6 weeks of age, mice were induced with adenovirus-Cre recombinase (Ad-Cre) by intratracheal intubation to allow cre-lox-mediated recombination of floxed *Rb1*, *p53* and *p130* alleles. For syngeneic orthotopic models, ultrasound-guided transthoracic injection was performed using 200,000 RPP631, RP or RPP-MYC cells in 30 µL PBS directly into the lung of 6 to 8-week-old C57BL/6 (Jackson Laboratory, Stock No: 000664). For OT-I T cell assay, OT-I mice were purchased from the Jackson Laboratory (Stock No: 003831). Both males and females mice were used and all mice were maintained in accordance with the respective NYULH and DFCI on the care, welfare, and treatment of laboratory animals. All experiments met or exceeded the standards of the Association for the Assessment and Accreditation of Laboratory Animal Care, International (AAALAC), the United States Department of Health and Human Services, and all local and federal animal welfare laws.

Cell Lines

Established mouse SCLC *Rb1*^{-/-}*p53*^{-/-}*p130*^{-/-} (RPP)631, *Rb1*^{-/-}*p53*^{-/-} (RP) and RPP-MYC cells were maintained in HITES medium ([Carney et al., 1981](#)) and confirmed by sequencing and western blotting ([Oser et al., 2019](#)). Human cell lines (GLC16, DMS79, NCI-H69, NCI-H82) were maintained in RPMI 1640 (Thermo Fisher Scientific). The HAP1 CDK7 WT and C312S cell lines ([Olson et al., 2019](#)) were cultured in IMDM media (Thermo Fisher Scientific). All cell line media were supplemented with 10% Fetal Bovine Serum (FBS, Sigma-Aldrich) and 1% penicillin/streptomycin (Thermo Fisher Scientific) and all cell lines were cultured in a humidified chamber with 5% CO₂.

METHOD DETAILS

Chemicals

YKL-5-124 was synthesized according to ([Olson et al., 2019](#)). THZ531 was synthesized according to ([Zhang et al., 2016](#)). THZ1 and Bio-THZ1 was synthesized according to ([Kwiatkowski et al., 2014](#)). Anti-PD-1 (clone 29F.1A12) was a kind gift from Dr. Gordon Freeman (DFCI).

In Vivo Toxicity Evaluation and Treatment Studies

For evaluation of *in vivo* toxicity of YKL-5-124, a dose-escalating study from 2.5 mg/kg to 15 mg/kg q.d. five times/week via intra-peritoneal injection (i.p.) was tested in C57BL/6 mice. *In vivo* toxicities including body weight and blood cell counts including platelet, red blood cells and white blood cells were monitored. Similarly, a separate cohort was used to evaluate *in vivo* toxicity of combining YKL-5-124 and anti-PD-1 in C57BL/6 mice.

For treatment studies, mice were evaluated by MRI imaging (Preclinical Imaging Laboratory, NYULH) to quantify lung tumor burden before for randomization and after drug treatment for efficacy evaluation. Mice were treated with either vehicle and isotype IgG (Control), anti-PD-1 200 µg/mouse (clone 29F.1A12), YKL-5-124 10 mg/kg, or combined anti-PD-1 and YKL-5-124 (Combo). YKL-5-124 was administered daily from Monday to Friday, and PD-1 antibody was administered three times a week (Monday, Wednesday, and Friday). For chemotherapy, cisplatin (5 mg/kg) was given on Day 1 and etoposide (10 mg/kg) on Day 1, 2, 3 every seven days per cycle for three cycles. For CD4 or CD8 neutralization study, mice were injected intraperitoneally with either αCD8 antibody (400 µg, Bio X Cell, clone 2.43), or αCD4 (400 µg, Bio X Cell, clone GK1.5), or IgG2b isotype control (400 µg, Bio X Cell, clone LTF-2) 48 and 24 h before beginning anti-PD-1 and YKL-5-124 (Combo) treatment, and every 4 days thereafter.

Cell Viability Assay

Cells were seeded in 96-well plates ($0.01\text{--}0.02 \times 10^6$ cells/well) in media and treated with YKL-5-124 at indicated concentrations and time points. Cell viability was measured using the MTS-based CCK-8 assay (Dojindo, Cat#CK04). Absorption at 450 nm was measured 3 hr after addition of CCK-8 reagent to cells.

Cell Cycle Analysis

Cells were seeded in 6-well plates ($0.5\text{--}1 \times 10^6$ cells/well) in media and treated with YKL-5-124 at indicated concentrations and time points. Cells were collected by centrifugation, washed in cold PBS and resuspended in 1 ml of 80% EtOH in PBS and stored overnight at -20°C . Cells were again collected by centrifugation and washed 3X with cold PBS. Hereafter cells were resuspended in PBS containing: 0.1% Triton X-100, 25 $\mu\text{g}/\text{ml}$ Propidium Iodide (PI) and 0.2 mg/ml RNase A and incubated for 45 min at 37°C . After incubation, cells were placed at 4°C until ready for analysis with flow cytometry. Cells were gated for PI staining and cell accumulation in G1, S and G2/M were calculated using ModFit LT software.

BrdU Analysis

Cells were seeded in 6-well plates ($0.5\text{--}1 \times 10^6$ cells/well) in media and treated with YKL-5-124 at indicated concentrations and time points. Prior to collection, cells were pulsed with 1 mM BrdU (BD Biosciences, #559619) for 2-4 hr (depending on cell line doubling time) and collected by centrifugation. Hereafter cells were permeabilized, fixated and stained according to BrdU kit instruction (BD Biosciences, Cat#559619). Cells were gated for BrdU incorporation (FITC) and 7-aminoactinomycin D (7-AAD) to quantify cells in G1, S (BrdU positive) and G2/M.

RNA Extraction and RT-qPCR

Cell pellets were collected and then subjected to total RNA extraction using RNeasy Plus Mini Kit (QIAGEN, Cat#74136) according to the manufacturer's instructions, or using TRIZol:Chloroform phase-separation by centrifugation followed by RNA precipitation using isopropanol. The extracted RNA was reversely transcribed into cDNA using the High-Capacity RNA-to-cDNATM Kit (Thermo Fisher Scientific, Cat#4387406) according to the manufacturer's instructions. The obtained cDNA samples were diluted and used for RT-qPCR. PowerUpTM SYBRTM Green Master Mix (Thermo Fisher Scientific, Cat#A25742) or TaqMan Gene Expression Master Mix (Life Technologies, Cat#4369514). Gene specific primers with sequences listed in [Table S1](#) were used for PCR amplification and detection on the StepOnePlusTM Real-Time PCR System (Thermo Fisher Scientific). RT-qPCR data were normalized to *Actb* (mouse cells) or *GUSB* (human cells) and presented as fold changes of gene expression in the test sample compared to the control.

Protein Extraction and Western Blotting Analysis

Cells in culture were collected by centrifuging at 1,500rpm and then washed with ice-cold PBS twice to completely remove residual medium. RIPA lysis buffer (Thermo Fisher Scientific, Cat#89900) supplemented with HaltTM Protease and Phosphatase Inhibitor Cocktail (Thermo Fisher Scientific, Cat#78440) was added to cell pellets to extract protein. Protein concentrations in lysates were measured by PierceTM BCA Protein Assay Kit (Thermo Fisher Scientific, Cat#23225) and followed by the addition of SDS loading buffer (6X) and heated at 95°C for 5 min. Equal amount of protein samples was subjected to 4-20% gradient gel SDS-PAGE and transferred to a nitrocellulose membrane (Bio-Rad, Cat#1704271). The membrane was blocked in Odyssey[®] Blocking Buffer (LI-COR, Cat#927-50003) at room temperature for 1 hour and incubated with appropriate antibodies at 4°C overnight ([Key Resources Table](#)). Antibodies were diluted in TBST (TBS with 0.1% Tween) with 20 % LI-COR Odyssey Blocking Buffer. On the next day, the membrane was washed with TBST (TBS with 0.1% Tween) four times and incubated with appropriate secondary antibodies (LI-COR, anti-Rabbit, Cat#925-32213; anti-Mouse, Cat#925-68072) at room temperature for 1 hour. Membranes were imaged using the LI-COR Odyssey[®] Imaging System.

Competitive Pull-down Assay for YKL-5-124 Target Engagement

Bio-THZ1 pull-down experiments followed by western blotting of enriched proteins was performed as described in ([Kwiatkowski et al., 2014](#)). Briefly, cells were treated with YKL-5-124 or DMSO for 6 hr (*in vitro*) or 72 hr (*in vivo*). Following treatment, cells were washed twice with cold PBS and then lysed in the following lysis buffer: 50 mM TrisHCl pH 8.0, 150 mM NaCl, 1% NP-40, 5 mM EDTA, 1mM DTT, and protease/phosphatase cocktails. Following clearance, lysates were treated with biotinylated THZ1 for pull-down overnight at 4°C . Lysates were further incubated at room temperature for 3 hr to increase the efficiency of covalent bond formation. Lysates were then incubated with streptavidin agarose for pull-down for an additional 2-3 hr at 4°C . Agarose beads were washed 5 times with lysis buffer and then boiled in 2X SDS at 95°C . SDS-page resolved precipitated proteins were probed for the indicated proteins.

Immunofluorescence Staining and Imaging

Before fixation, cells in PBS were seeded for 30 min on 0.01% Poly-lysine coated coverslip. Cells were then fixed in 4% paraformaldehyde (Diluted the 32% paraformaldehyde in PBS, Electron Microscopy Sciences 15714) for 10 min at room temperature. Cells were washed three times for 5 min with 200 mM glycine containing PBS, followed by permeabilization with 0.3% Triton X-100 in PBS for 15 min. After blocking with 5% bovine serum albumin (BSA) in PBS for 1 hour, cells were incubated with primary antibody (γ H2A.X, Cell signaling 9718, 1: 200) diluted in a 5% BSA in PBS solution overnight at 4°C . After washing four times with PBS, cells

were incubated with Alexa Fluor Plus 555 (Invitrogen A32732, 1: 500) secondary antibody for 1 hour and washed three times with PBS. Cell nuclei were counterstained with DAPI (BioLegend 422801, diluted to 600nM in PBS) for 5 min. Cells were washed two more times in PBS before mounting with Fluorescence Mounting Medium (Dako, S3023). Images were acquired using Zeiss 880 Laser Scanning Confocal Microscope and were processed by FIJI (NIH). Micronucleus were identified manually by distinct DAPI staining outside the main nucleus.

EdU and MCM2 Imaging by the Stochastic Reconstruction Microscopy (STORM)

Sample Preparation

RPP631 cells were incubated in the presence of 100nM YKL-5-124 for 48-72 hr. EdU was pulsed during the last 30 minutes of YKL-5-124 treatment. Treated cells were pre-extracted using 0.5% Triton in CSK buffer (10 mM Hepes, 300 mM Sucrose, 100 mM NaCl, and 3 mM MgCl₂, pH = 7.6) for 10 minutes, and fixed with paraformaldehyde (4%) for 30 minutes. Cells were then rinsed 3 times with PBS and blocked (2% glycine, 2% BSA, 0.2% gelatin, and 50mM NH₄Cl in PBS) overnight at 4°C for further staining. EdU was tagged with Alexa Fluor 647 picolyl azide through Click reaction (Thermo Fisher, C10640) before immunofluorescent labeling of target proteins, for which the antibodies are mouse anti-PCNA (Santa Cruz Biotech., sc56, 1:1000), goat anti-mouse (Alexa Fluor 750 conjugated, Thermo Fisher, A-21039, 1:5000), and rabbit anti-MCM2 (Alexa Fluor 647 conjugated, Abcam ab223403, 1:500). Fixed cells were mounted onto microscope glass for STORM imaging in freshly mixed imaging buffer (1 mg/mL glucose oxidase (Sigma-Aldrich, G2133), 0.02 mg/mL catalase (Sigma-Aldrich, C3155), 10% glucose (Sigma-Aldrich, G8270), and 100 mM cysteamine (MEA, Fisher Scientific, BP2664100).

Optics

STORM imaging was performed on a customized inverted microscope as described previously ([Yin et al., 2019](#)). In brief, the 639 nm laser (UltraLaser, MRL-FN-639-800) was collimated and reflected into the TIRF Objective (HCX PL APO 63X NA = 1.47, Zeiss), and the adjusted illumination power is ~ 1.5 kW/cm². A 405 nm Laser line (MDL-III-405-150, CNI) was equipped to reactivate Alexa Fluor 647 fluorophores. A 750 nm laser (UltraLaser, MDL-III-750-500) was also applied to illuminate Alexa Fluor 750 labeled PCNA for S-phase cell selection. Cell samples were sequentially illuminated with 639 and 750 laser lines and the emitted fluorescence was collected by the same objective with a 2X magnification tube lens (Diagnostic Instruments). The fluorescence was then filtered by single band filters (Semrock FF01-676/37 and FF02-809/81), switched in a filter wheel accordingly. Photons were eventually fed to a sCMOS camera (Photometrics, Prime95B) and collected at 33 Hz, 2000 frames for an image stack.

Single-molecule Localization and Pair-Correlation Analysis

Each 2000-frame single-molecule image stack was submitted to a home-built software for precise single-molecule localization. Briefly, each frame from an image stack was box filtered, roughly-local-maxima-localized, segmented, and submitted to GPU for Point-Spread-Function (PSF) fitting using the Maximum Likelihood Estimation (MLE). The fitting accuracy was evaluated using Cramer-Rao Lower Bound (CRLB). Note that the patterned read-out noise of the sCMOS camera was calibrated before imaging. Such read-out noise for each pixel was approximated into a Gaussian distribution and convolved with the Poisson shot noise for MLE fitting ([Huang et al., 2013](#)). The generated coordinates were then submitted for Auto-Pair-Correlation analysis to estimate the nuclear density of the fluorophores within a nucleus, as well as how many fluorophores are on average in each EdU/MCM2 focus ([Sengupta et al., 2011; Veatch et al., 2012](#)). The number of fluorophores is proportional to the quantity of EdU and MCM2. This method empowered us to map the precise molecular coordinates of EdU and MCM2 molecules within a cell with a resolution of ~10 nm, and to extract robust metrics such as the amount of EdU and MCM incorporated per nucleus as well as their quantity within each focus.

Histology and Immunohistochemistry

Lungs were perfused with 10% formalin, stored in fixative overnight, and embedded in paraffin. Four-micron thick sections of formalin fixed tissue were used for immunoperoxidase analysis after baking at 60°C for 1 hour, deparaffinization and rehydration (100% xylene X4 for 3 minutes each, 100% ethanol X4 for 3 minutes each and running water for 5 minutes). The sections were blocked for peroxidase activity with 3% hydrogen peroxide in methanol for 10 minutes and washed under the running water for 5 minutes. The sections with pressure cooked (Biocare Medical) antigen retrieval were at 120°C in Citrate Buffer (Dako Target Retrieval Solution, S1699). The slides were cooled for 15 minutes, and transferred to Tris buffer saline (TBS). The sections were incubated with rabbit monoclonal anti-MYC (Abcam Cat#ab32072; 1:900) and/or rabbit monoclonal anti-ASCL1 antibody (Abcam Cat#ab211327; 1:100) for 40 min room temperature. The secondary antibody was used Leica Novolink Polymer (Cat#RE7161) 30 min incubation. All the incubations were carried out in a humid chamber at room temperature. The slides were rinsed with TBS in between incubation. The sections were developed using 3,3'-diaminobenzidine (DAB) as substrate and counter-stained with Mayer's Hematoxylin.

Luminex Analysis of Murine BAL Fluid

Mouse lung bronchoalveolar lavage (BAL) was performed by intratracheal injection of 2 mL of sterile PBS followed by collection by aspiration. TNF α , CXCL9 and CXCL10 levels were measured using mouse Cytokine/Chemokine 32-plex Assay (MILLIPLEX, Millipore) on Luminex® SD system (Luminex). Concentrations (pg/mL) of each protein were derived from 5-parameter curve fitting models according to the manufacturer's instructions.

MRI Quantification

Animals were anesthetized with isoflurane to perform MRI of the lung field using BioSpec USR70/30 horizontal bore system (Bruker) to scan 24 consecutive sections. Tumor volumes within the whole lung were quantified using 3-D slicer software to reconstruct MRI volumetric measurements as described previously (Christensen et al., 2014). Acquisition of the MRI signal was adapted according to cardiac and respiratory cycles to minimize motion effects during imaging.

Immune Profiling Flow Cytometry

Mice were humanely euthanized, and mouse lungs were perfused using sterile PBS through heart perfusion from the left ventricle after BAL fluid collection. The whole lung was cut and minced into small pieces followed by digestion in collagenase D (Sigma-Aldrich) and DNase I (Sigma-Aldrich) in Hank's Balanced Salt Solution (HBSS) at 37°C for 30 minutes. After incubation, the digested tissue was subjected to a 70 µm cell strainer (Thermo Fisher Scientific) to obtain single-cell suspensions. Separated cells were treated with 1× red blood cell (RBC) lysis buffer (BioLegend). Live cells were determined by LIVE/DEAD fixable aqua dead cell stain kit (Molecular Probes). The cell pellets were resuspended in PBS with 2% FBS for FACS analysis. Cells were stained with cell surface markers as indicated followed by fixation/permeabilization (eBioscience). Cells were imaged on BD LSRII (BD Biosciences) and analyzed using FlowJo software (Tree Star).

Ex Vivo OT-I T Cell Assay

The spleen of OT-I mice was minced with a razor and mashed through a 40 µm strainer to form a single-cell suspension. Separated cells were then treated with RBC lysis buffer and a number of 5×10^5 cells were seeded in a 96-well U-bottom plate. For conditioned medium culture assay, RPP631 cells were treated with either DMSO or YKL-5-124 for 48 hr and drug was washed off after first 6-hour treatment. Subsequently, DMSO-conditioned medium or YKL-5-124-conditioned medium were collected and added to above single-cell suspension in a 96-well U-bottom plate in the presence of Ova_{257–264} peptide (10 µg/ml, GenScript, Cat#RP10611) for 4 days as previously described (Barilla et al., 2019). Alternatively, DMSO or YKL-5-124 was added directly to single-cell suspension in the presence of Ova_{257–264} peptide for 4 days in the T cell assay medium (complete RPMI with HEPES, sodium pyruvate, MEM non-essential amino acids and 2-mercaptopethanol). T cell activation markers CD69, TNFα and IFNγ were analyzed by flow cytometry.

Generation of cGAS CRISPR/Cas9 Knockout

Single guide RNA (sgRNA) oligonucleotides (Sigma-Aldrich) targeting cGAS (Table S1) were cloned into lentiviral expression vector lentiCRISPR v2 (Addgene #52961). Lentivirus was generated by transfection of HEK-293T cells with lentiCRISPR v2, or lentiCRISPR v2-sgcGAS and the packaging plasmids psPAX2 (Addgene #12260) and pMD2.G (Addgene #12259) using Lipofectamine 3000 (Thermo Fisher Scientific). Viral particles released into the cell culture supernatant were filtered with 0.45-µm filters and added to target cells.

Bulk-RNA Sequencing Analysis

Paired-end reads were aligned to mouse mm10 genome using STAR (v2.5.2b) (Dobin et al., 2013). Reads with good mapping quality (MAPQ > 30) that aligned to genomic exons were counted using featureCounts (Liao et al., 2014) (mm10 Ensembl 93) to generate a table with counts for each gene. Differential gene expression analysis was performed using the R package DESeq2 (Love et al., 2014) using the IfcShrink function. Genes with false discovery rate (FDR) lower than 0.05 were considered significantly differentially expressed. Gene set enrichment analysis (GSEA) (Subramanian et al., 2005) was performed on a list of genes ranked from high to low DESeq2 estimated fold-change using the GSEAPreRanked function with enrichment statistic classic and 1000 permutations.

Single-Cell RNA Sequencing

Experimental Protocol and Library Generation

To account for interindividual variability, we harvested pooled fresh tumor-bearing lungs from two mice in two independent cohorts of RPP orthotopic mice which were treated with control, YKL-5-124, anti-PD-1 and combination treatment for seven days. Single cell suspensions were achieved as described above and were sorted using DAPI staining. Cells were then resuspended into single cells with 0.4% BSA for 10x genomics processing. Cell suspensions were loaded onto a 10x Genomics Chromium instrument to generate single-cell gel beads in emulsion (GEMs). Approximately 5,000 to 10,000 cells were loaded per channel. scRNA-seq libraries were prepared using the following Single Cell 3' Reagent Kits: Chromium™ Single Cell 3' Library & Gel Bead Kit v2 (PN-120237), Single Cell 3' Chip Kit v2 (PN-120236) and i7 Multiplex Kit (PN-120262) (10x Genomics, Pleasanton, CA, USA) as previously described (Zheng et al., 2017), and following the Single Cell 3' Reagent Kits v2 User Guide (Manual Part # CG00052 Rev A). Libraries were run on an Illumina HiSeq 4000 system (SY-401-4001, Illumina) as 2 x 150 paired-end reads, one full lane per sample, for approximately >90% sequencing saturation.

Data (Pre-)processing

The Cell Ranger Single Cell Software Suite, version 1.3 was used to perform sample de-multiplexing, barcode and UMI processing, and single-cell 3' gene counting. A detailed description of the pipeline and specific instructions to run it can be found at: <https://support.10xgenomics.com/single-cell-gene-expression/software/pipelines/latest/what-is-cell-ranger>. A high quality gene expression matrix was created in sequential preprocessing steps as provided in the Seurat (v2.3.4) pipeline (Butler et al., 2018). First only genes that were detected in both independent scRNAseq datasets were retained and cells were excluded if respectively

more than 0.2% or 0.3% of detected genes were from mitochondrial or ribosomal origin or if less than 500 genes were detected. The count matrix was subsequently log-normalized with a scale-factor of 10000 and the obtained normalized matrix was further corrected by retaining the residuals after regressing out systematic changes due to number of detected UMIs, percent genes from mitochondrial or ribosomal origin.

Clustering and Annotation

Cells from both independent datasets were merged together in canonical correlation (CC) space using the intersection of highly variable genes, identified as genes with higher-than-expected variability in consecutive ranked expression bins, from both datasets. The implementation of CC alignment and selection of downstream dimensions to use was performed as described in the *Seurat* package. Cells were clustered using the Louvain algorithm based on a shared nearest-neighbor network. The final resolution of all subsequent clustering analyses was determined by the biological questions and the need for coarse or fine-grained detail as explored in the subsequent cluster annotation. Clusters were annotated using input from multiple sources, we i) calculated a stromal, cancer and immune score using the *estimate* (v1.0.13) package (Yoshihara et al., 2013) in R, ii) identified cluster specific gene expression markers based on gini-scores, iii) created a hierarchical tree based on Pearson correlation scores between clusters to visualize lineage relationships and iv) compared clusters to those of the Immgen database using the *SingleR* (v0.2.1) package (Aran et al., 2019) in R. UMAP as implemented by the *uwot* (v0.0.0.9010) package in R was used to visualize clusters in 2D CC space. Overall this strategy was hierarchically used to assess all cells, cancer cells only, immune cells only and finally T-cells only.

Quality Control

In the first clustering step, several additional analyses were performed to remove dubious or non-reproducible clusters from downstream analyses. To identify contamination of immune cell clusters with cancer cells we performed k-means (2 centers) clustering on all cells on identified and known canonical markers (*Epcam*, *Calca*, *Stmn1*, *Ascl1*, *Krt7*, *Nfib*, *Krt8*, *Krt18*) specific to cancer cells. Single-cell outliers with high expression of the aforementioned cancer genes were marked using a density based clustering algorithm using the *dbscan* (v1.1-3) R package. Similarly, at the cluster level, immune cell clusters with high expression of aforementioned cancer genes were split and labeled as cancer-contaminated and cancer-free cells. Furthermore, clusters that represent doublets were identified using the *doubletCluster* function of the *scran* (v1.10.1) (Lun et al., 2016) and *scater* (v1.10.0) (McCarthy et al., 2017) package in R and concomitantly observing a significant distribution shift for total number of detected UMIs per cell. To detect non-reproducible clusters between datasets we compared changes in distribution and only removed a cluster if this cluster was only observed in all treatment conditions of only one dataset with all individual z-scores greater than 3. Together all marked single-cells identified in any of the previous quality analyses were removed from further analyses.

Cell-Cycle Analysis

Cells were first classified in G1, G2/M or S categories using the *Cyclone* function in the *scran* package (Scialdone et al., 2015) in R, which provides a discrete grouping based on genes known to be specific to the specific cell-cycle phases. To infer more continuous cell-cycle states we first identified the top 50 genes that are associated with each cell-cycle phase by performing pairwise comparisons using the *limma* (v3.38.2) package in R (Ritchie et al., 2015). Based on those cell-cycle phase specific genes we calculated a G1, G2/M and S-score for each cell by summarizing the normalized expression values. All cells were subsequently clustered by k-means in eight groups using the three cell-cycle scores. We selected eight groups since there are at least three cell-cycle states and each cell could be considered inside (high score) or outside (low score) a state ($2^3 = 8$). To visualize the continuous cell-cycle progression states the median of each group was visualized in a 3D plots and nearest neighbors were connected. The 3D visualization was projected in 2D by rescaling the average of each k-means group between 0 and 1. To assess changes in cell-cycle progression state distribution upon treatment we calculated the percentage of single-cells within each group for each treatment condition and compared that to vehicle-treated samples.

Gene Set Enrichment Analysis

GSEA (Subramanian et al., 2005) was performed on a list of genes ranked according to *limma* PI-values (-log10(adjusted p-value) x absolute logFC), using the *GSEAPreRanked* function with enrichment statistic classic and 1000 permutations. For specific enrichment of superenhancer-associated genes found in (Christensen et al., 2014), a custom gene set for those genes was first created and merged with in the GO BP category of the MSigDB database to obtain the enrichment ranking. Specific gene enrichment within a cluster was visualized by averaging the expression of each gene per cluster and subsequently rescaling z-scores for each gene between -1 and 1.

CD4⁺ and CD8⁺ T-Cell Identification

To identify CD4⁺ and CD8⁺ subgroups within the annotated T-cell cluster, we first over-clustered, to mitigate known dropout effects in single-cell data, the T-cell population and divided all subclusters in CD4⁺ or CD8⁺ using k-means clustering (groups = 2) based on the expression of *Cd4* and *Cd8a*. This provided a clear separation between predominant CD4⁺ and CD8⁺ cells. scRNAseq uncovered five distinctive clusters of CD4⁺ T cells (c1, c4, c5, c6 and c7) and seven clusters of CD8⁺ T cells (c0, c3, c5, c7, c8, c9 and c10). Among these, functionally defined clusters c5 and c7 are comprised of both CD4⁺ T cells and CD8⁺ T cells.

CD4⁺ T Cells

Cells in c1 expressed high levels of *Cd4* and the naive T cell marker *Sell* (CD62L), but lacked the expression of effector/memory T cells marker *Cd44* and T cell activation genes, including *Ifng*, *Icos*, *Lag3*, *Havcr2* (*Tim-3*), *Pdcd1*, *Tnfrsf4* and *Ctla4*. c1 appeared to be naive T cells. c5 showed the highest levels of activated markers such as *Icos*, *Tim-3*, *Ctla4* and *Pdcd1*, and intermediate levels of *Sell* and *Cd44*, representing an activated/effector T cell signature. c4 expressed much lower levels of these activation markers, and lower *Sell* and higher *Cd44*. c6 cells expressed high levels of *Cd4* and *Foxp3*, which are classic markers for regulatory T cells (Tregs). These cells

also expressed intermediate levels of T cell activation genes *Icos*, *Ctla4* and *Pdcd1*. c7 displayed highest levels of *Cd44* and low levels of *Sell*, intermediate levels of T cell activation markers such as *Icos*, *Tim-3* and *Pdcd1*, indicating an effector/activation T cell signature.

CD8⁺ T Cells

Both c0 and c8 expressed high levels of *Cd8a* and naive T cell marker *Sell*, but low levels of *Cd44* and T cell activation genes *Lag3*, *Tim-3*, *Pdcd1*, *Ifng*, *Icos*, *Tnfrsf4* and *Ctla4*. c9 expressed intermediate level of *Sell* and relatively low levels of the T cell activation genes. Thus, c0, c8 and c9 appeared to be naive-like cells and in an inactivated state. c3 expressed high levels of *Cd8a* and memory T cell marker *Klrg1*, intermediate levels of cytotoxic T cells marker *Gzma* and *Gzmb*, and intermediate levels of two central T cell differentiation genes *Tbx21* (T-bet) and *Eomes*. This cluster of CD8⁺ T cells is thought to represent “memory” population with cytotoxicity and low proliferation capability. c10 showed the highest levels of T cell activation genes *Lag3*, *Tim-3*, *Pdcd1*, *Tnfrsf18* and *Ifng*, and cytotoxic markers *Gzma*, *Gzmb* and *Prf1*, suggesting these cells are fully differentiated CTLs. c5 expressed low levels of *Sell* but high levels of effector T cell marker *Cd44* and activation markers *Icos*, *Ctla4* and *Tnfrsf4*, representing an “effector” T cell signature. c7 cells expressed high levels of *Mki67* are comprised of a mixture of CD4⁺ T cells and CD8⁺ T cells, highlighting their cell proliferation capability. In addition, c5 is another functionally defined cluster of effector/activated T cells, which contain both CD4⁺ and CD8⁺ T cells.

Illustration Tool

The graphical abstract image is created with BioRender.

QUANTIFICATION AND STATISTICAL ANALYSIS

Statistical analyses were performed using GraphPad Prism 7 software and statistical significance was determined by $p < 0.05$. Data are presented as mean with SD unless otherwise specified. Statistical comparisons were performed using unpaired Student t test for two-tailed p value unless otherwise specified (* $p < 0.05$, ** $p < 0.01$, *** $p < 0.001$, **** $p < 0.0001$).

DATA AND CODE AVAILABILITY

The accession number for the raw and processed data of bulk RNA sequencing and single-cell RNA sequencing generated and reported in this paper is GEO: GSE129299.